

# Elongated bubble centring and high-viscosity liquids in horizontal gas-liquid slug flow: Empirical analyses and novel theory

Sean J. Perkins

<sup>a</sup>*University of Alberta, Department of Civil & Environmental Engineering and the School of Mining & Petroleum Engineering, 116 St and 85 Ave, Edmonton, T6G 2R3, Alberta, Canada*

---

## Abstract

Elongated bubble centring—an obscure counter-buoyant phenomenon encountered in horizontal gas-liquid slug flow—is correlated with liquid viscosity and their connection is theorized. Extracting from three sets of high-viscosity liquid (HVL) photographic data with  $\mu_L \in [1, 960]$  mPa s and  $D \in [20, 50.8]$  mm, the degree of incurred centring is found to increase, generally, in proportion to  $\mu_L$  for a wide range of operational rates as evidenced through measurements at bubble nose, body and tail. It is demonstrated that full and nearly-symmetric centring can occur in HVL-containing flows—the former at relatively low inertial supply in contradiction to water-based dynamics. Qualitative advancements regarding the mechanistic nature of bubble centring and its plausible function within flow pattern transition theory are presented. Elaborating on recent modelling efforts, four distinct hypotheses are formulated: 1) film region laminarity as a modulator for centring; 2) boundary layer theory in slug flow to differentiate an outer-layer, relative motion-dominated film flow necessary for the initiation of centring; 3) wedge theory—a plausible alternative mechanism for partial-centring; and 4) a novel framework for the slug-annular transition composed of two unique mechanisms—centring and coalescence. The postulated boundary layer theory is investigated using a calibrated case of HVL slug flow and a dynamical environment conducive to centring mechanism proliferation is calculated.

**Keywords:** Bubble centring, High-viscosity liquids, Slug flow, Horizontal pipe, Slug-annular transition, Boundary layer theory

---

## Contents

<b>1</b>	<b>Introduction</b>	<b>2</b>
<b>2</b>	<b>Methodology</b>	<b>7</b>
2.1	Data curation . . . . .	7
2.2	Model derivation . . . . .	15
<b>3</b>	<b>Results</b>	<b>18</b>
3.1	Empirical observation . . . . .	18
3.2	Correlational analysis . . . . .	30
<b>4</b>	<b>Theory</b>	<b>33</b>
4.1	Centring mechanics . . . . .	33
4.2	Boundary layer theory . . . . .	38
4.3	Wedge theory . . . . .	49
4.4	The slug-annular transition . . . . .	51
<b>5</b>	<b>Finalities</b>	<b>58</b>
5.1	Conclusions . . . . .	58
5.2	Future work . . . . .	60
<b>Appendix A</b>	<b>Extracted data</b>	<b>62</b>
<b>Appendix B</b>	<b>Additional centring plots</b>	<b>63</b>
<b>Appendix C</b>	<b>List of acronyms</b>	<b>65</b>

## 1. Introduction

Concurrent flow of gas and liquid in a circular pipe yields a complex system featuring multilayered dynamic behaviour. Depending on pipe, fluid and operational parameters, various discrete geometric configurations—known as flow patterns—may be observed. In a horizontally-oriented system, primary flow patterns include: stratified (smooth or wavy), intermittent (plug or slug), annular and dispersed bubble flows (Taitel et al., 1978). Accurate prediction and modelling of flow patterns is supremely important in the preservation of engineering feasibility. Multiphase pipe flow phenomena such as heat transfer,

pressure distribution and mechanical fatigue are captured using flow pattern-specific methodologies; therefore, a robust, validated conceptual paradigm is necessary to ensure competent design protocol in petroleum, processing and nuclear industries where such flow-types are commonplace. Transitional boundaries which differentiate flow patterns are of tantamount theoretic interest to the intrinsic physicality that defines them; as such, considerable efforts have been dedicated to understanding the nature of flow pattern conversion. Historic empirical works include [Lockhart and Martinelli \(1949\)](#), [Baker \(1954\)](#) and [Mandhane et al. \(1974\)](#) while the analytic endeavours of [Taitel and Dukler \(1976\)](#) represent a baseline reference of mechanistic inquiry.

To foster economic sustainability in the global energy sector, efficient production and transportation of heavy oil resources is critical. Due to intricate rheology and chemical constituency, hydrocarbon liquids pose a unique challenge to both researchers and operators. Notably, they are characterized by a remarkable range of potential viscosity values; for example, under in situ conditions, certain crude oils may have  $\mu_L < 1\text{mPa}\cdot\text{s}$  whereas others are found with up to  $\mu_L = 100,000\text{mPa}\cdot\text{s}$  while remaining flowable ([Islam, 2023](#)).<sup>1</sup> Viscosity—a fluid’s internal resistance to deformation—is proportional to the structural complexity of composing molecules; subsequently,  $\mu_L$  is a function of temperature, pressure and solution-gas since all three affect positioning of hydrocarbon chains ([McCain, 1990](#)).

Compared to otherwise equivalent water-based systems, gas-liquid pipe flows involving a high-viscosity liquid (HVL) are known to exhibit a variety of macroscopic peculiarities ([Zhang et al., 2012](#)).<sup>2</sup> Furthermore, these flow-types are ubiquitous in the realm of practical application; for instance, pipelined flow of heavy oil is often accompanied by hydrocarbon gases, stemming either organically from the reservoir or flashed from a miscible solution below a pressure threshold known as the bubble point. Gas-HVL pipe flow can also emerge during enhanced oil recovery schemes which utilize injected steam to mobilize bitumen—a naturally existing semi-solid with  $\mu_L > 1,000,000\text{mPa}\cdot\text{s}$  ([Islam, 2023](#))—into a flowing commodity, particularly when live steam enters producer wells after breaking through highly-permeable reservoir trajectories ([Dong et al., 2021](#)). Consequently, relevant theoretical explorations have

---

<sup>1</sup>With respect to typical oilfield units,  $1\text{mPa}\cdot\text{s} = 1\text{cp}$ .

<sup>2</sup>HVL: high-viscosity liquid; defined here broadly as a liquid with  $\mu_L > 1\text{mPa}\cdot\text{s}$ . This is not a universal definition—in this context, an HVL is any liquid more viscous than water. However, conclusions derived here apply only for HVL-systems with  $\mu_L \geq 5.5\text{mPa}\cdot\text{s}$ .

matured into a popularized area of research which lends itself to the facilitation of heavy oil resource extraction.

Over the last two decades, the study of gas-HVL flow patterns in horizontal pipes has benefited from a marked influx of experimental publication (Gokcal et al., 2008; Matsubara and Naito, 2011; Al-Safran et al., 2013; Zhao et al., 2013; Al-Safran et al., 2015; Zhao et al., 2015; Al-Safran and Al-Qenae, 2018). Evidently, the subfield’s contemporary status is primarily one of empiricism and speculation. Lacking is a base of purely theoretical works which query fundamental phenomenology corresponding to the introduced presence of an HVL. Invoking the aforementioned model from Taitel and Dukler (1976) (TD76)—which provides a mechanistic framework for steady-state flow pattern formation in horizontal gas-liquid pipe flows—the situation is exemplified.<sup>3</sup> TD76 is widely accepted and thoroughly validated for water-predicated flows (Shoham, 2006); further, because it dissects individual boundaries, seemingly, into their most rudimentary components, it is considered to be a foundational explanation for flow pattern transition phenomena. However, a problem is encountered when implementing TD76 for the prediction of HVL flow pattern data; for example, inputting laboratory results from Matsubara and Naito (2011) and Zhao et al. (2013) indicates that modelling efficacy diminishes exponentially with increasing  $\mu_L$ , in certain cases demonstrating null predictability—shown here in figure 1.

As is discussed in §4.4, other papers—such as Gokcal et al. (2008)—have reported wide margins of predictive discrepancy for HVL data, even when utilizing mechanistic models alternative to TD76. Since these models are non-empirical, it is clear that imposing an HVL in a horizontal gas-liquid pipe flow induces a profound shift in underlying physics—particularly for  $\mu_L \gg 1$ . This divergence is precisely motivation for the present study. Ideally, existing data-based efforts will be transmuted into a cohesive, comprehensive narrative which describes exactly the implications of HVL-inclusion. A similar evolution happened in the 1970s when researchers harnessed a culmination of air-water data to craft a working framework of governing mechanics—a period designated the “awakening years” by Shippen and Bailey (2012). I hypothesize here that an analogous era is unfolding in the pursuit of knowledge for HVL-based flow dynamics—within which the genesis phase has arrived—and that

---

<sup>3</sup>TD76: Taitel and Dukler (1976) steady-state flow pattern transition model for horizontal gas-liquid pipe flows.

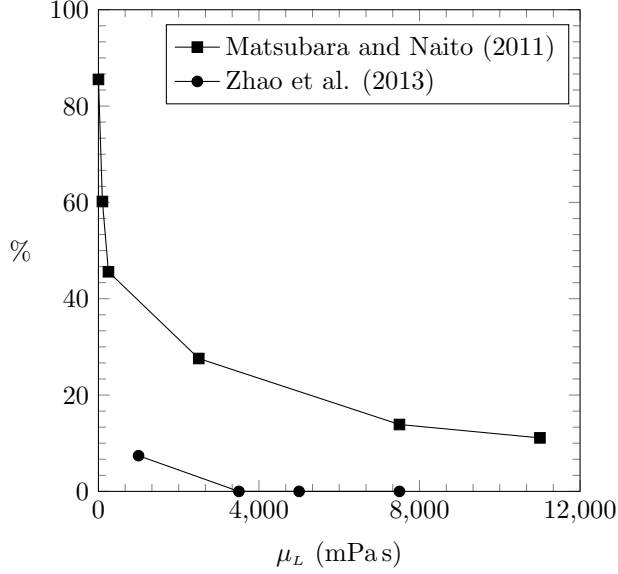


Figure 1: Predictive capability of the [Taitel and Dukler \(1976\)](#) (TD76) flow pattern transition model applied to HVL data from [Matsubara and Naito \(2011\)](#) and [Zhao et al. \(2013\)](#). %-values represent portion of total flow pattern points correctly determined.

an obscure flow event known as elongated bubble centring will prove itself an invaluable keystone in the course of this transformation.

Bubble centring is a counterintuitive element of horizontal gas-liquid slug flow—a heterogeneous flow pattern in which elongated bubbles and liquid slugs flow in alternating sequence ([Taitel and Barnea, 1990](#); [Dukler and Hubbard, 1975](#)). Typically, long bubbles flow flush to the upper pipe wall while a slower-moving liquid film flows beneath; however, under certain conditions, at least part of the bubble—starting from its nose or most downstream point—detaches from the upper pipe wall in defiance of natural buoyant proclivities. This effect was first discussed by [Bendiksen \(1984\)](#) who discovered that, in air-water systems, centring initiates when the flowing phases reach a critical value of Froude number—a metric which measures the balance of inertial and gravitational forces given by

$$Fr = \frac{u_m}{\sqrt{gD}} \quad (1)$$

where  $u_m = u_G^s + u_L^s$  is mixture velocity or the summation of gas and liquid superficial velocities and  $D$  is pipe diameter. In the first strictly mechanistic

study of its kind, Perkins and Li (2020) (PL20) provided a thorough theoretical evaluation of long bubble centring, including a simplistic model which calculates its operational manifestation, validated using externally generated visual data from air-water experiments.<sup>4</sup> In doing so, it was determined that centring is not only a function of  $Fr$  but of the ratio between gas and liquid superficial velocities, defined as

$$\gamma \equiv \frac{u_G^S}{u_L^S} = \frac{Q_G}{Q_L} \quad (2)$$

where  $Q_P$  is input volumetric flow rate of phase- $P$ . PL20 postulates that bubble centring is crucially important in the systemic architecture of HVL slug flow, reasoned in part due to prior researchers' observation of a thin liquid film above the elongated bubble in HVL systems (Zhao et al., 2015; Zhang et al., 2012) and from the obvious applicability of a singular utilized modelling simplification; namely, the existence of negligible turbulence (i.e., laminarity) throughout the underlying liquid film such that unbroken streamlines of relative motion can form—adjacent to the gas-liquid interface—long enough for a downward force to be transmitted due to a pressure differential and Bernoulli's principle.<sup>5</sup> In amplifying liquid viscousness, there is, in general, a decreasing probability of turbulence production; thus, for HVL flow systems, this vital assumption is more likely to be valid in contrast to air-water flows of otherwise same design.

Fortuitously, high-resolution photographic data which elucidate the correlative role of liquid viscosity in the dynamics of bubble centring have recently been published. Documented in this paper, these images were extracted from their original sources and analyzed thoroughly. The resultant illustration shows that the degree of centring incurred during horizontal slug flow is indeed a positively increasing function of  $\mu_L$ , thereby supporting theoretical musings put forth in PL20. Further, it provides a perfect segue for the creation of a mechanistic framework which qualitatively describes causality, implications and theoretical extensions relevant to the centring phenomenon and HVLs.

---

<sup>4</sup>PL20: Perkins and Li (2020) mechanistic bubble centring study.

<sup>5</sup>Accurate prediction of the centring phenomenon is important from a design perspective in that film region pressure differential will be under-valuated without consideration of detached bubble regions, as discussed in PL20. Since centring increases liquid-wall contact area, this effect is more pronounced in HVL systems because frictional forces and thus pressure losses are proportional to  $\mu_L$ .

In light of this opportunity, the present paper is dual-purpose: §§2 and 3 present implemented methodology, garnered relationality and established results based on experimentalism while §4 is devoted to expounding novel theories related to bubble centring and its phenomenological placement in the greater sphere of flow pattern transition philosophy. To summarize, the objectives of this study are threefold:

1. To provide a comprehensive analytical breakdown of raw elongated bubble centring data implicitly provided by Naidek et al. (2023), Shin et al. (2024) and Kim et al. (2020), including potential anomalies and operational dependencies on liquid viscosity, mixture Froude number and, where available, superficial velocity ratio;
2. To construct a container of logical, verifiable hypotheses that—in combination with integrated known theory—attempt to characterize the mechanistic nature of bubble centring as it relates to gas-HVL flow physics in horizontal pipes; and
3. To offer guidance and suggest specific, feasible required future work designed to reliably expand and advance the field of HVL multiphase pipe flow theory, consequently assisting in the optimization of heavy oil production and distribution.

## 2. Methodology

### 2.1. Data curation

Emerging as a research trend is the production and publication of high-resolution still-images which showcase the internal workings of multiphase pipe flows. Undoubtedly, the topological complexity inherent in such flows poses a significant challenge, necessitating improved capacities in photography and visual data processing; for example, a study by Widyatama et al. (2018) demonstrates a growing joint interest between multiphase fluid dynamicists and signal processing engineers.

Here, three peer-reviewed sources of pictorial data are studied, all of which offer compelling snapshots of the bubble centring phenomenon in horizontal gas-liquid slug flow generated from systems with liquid dynamic viscosity ( $\mu_L$ ) values larger than that of water (i.e., HVLs). For the sake of clarity, each dataset is assigned a short-form label and simplified set notation is used to differentiate isolated flow-cases. Table 1 outlines  $\mu_L$ -range,  $Fr$ -range, number of cases  $N$ , set notation, pipe diameter  $D$  and abbreviation used for the three

	Naidek et al. (2023)	Shin et al. (2024)	Kim et al. (2020)
Abbrev. $N$	<b>N23</b> 30	<b>S24</b> 5	<b>K20</b> 3
Set notation	<b>i.j</b> $i \in [1, 5] \in \mathbb{Z}$ $j \in [1, 6] \in \mathbb{Z}$	<b>m.k</b> $m \in \{A, B, C\}$ $k_{A,B} \in \{1, 2\}$ $k_C = 1$	<b><math>\Omega.q</math></b> $q \in [1, 3] \in \mathbb{Z}$
$\mu_L$ (mPa s)	$1 \rightarrow 30.4$	$37.7 \rightarrow 352$	$510 \rightarrow 960$
$Fr$	$1 \rightarrow 4$	$0.68 \rightarrow 3.23$	$0.57$
$D$ (mm)	26	20	50.8
$\rho_L$ (kg/m <sup>3</sup> )	$997.1 \rightarrow 1188$	$878 \rightarrow 970$	$846.6 \rightarrow 852.8$
$\sigma$ (mN/m)	$64.9 \rightarrow 73.2$	$19.4 \rightarrow 26.8$	33

Table 1: Relevant parameterization and notation for data sources utilized in this study.

datasets, along with liquid density  $\rho_L$  and surface tension  $\sigma$ .<sup>6</sup> Included are a total of  $N_{\Sigma} = 38$  cases across a liquid viscosity spectrum of  $\mu_L \in [1, 960]$  mPa s, all displaying variable degrees of observable long bubble centring. Other than N23’s  $\{1.j \mid \forall j\}$ —the referential water baseline—all cases considered are herein classified as HVL-containing.<sup>7</sup>

To retrieve centring data from supplied photos, rigorous analyses were performed using open-source, vectorized graphics software Inkscape (v.1.3.2) which offers exceptional resolution and, by proxy, measurement capabilities. Although the data have, technically, already been published in raw plainness, the incurred extent of bubble centring was not formally investigated, nor was it measured and correlated to metrics such as  $\mu_L$  and  $\gamma$ . Observations made through eyesight are inadequate; typically, high levels of magnification are required to properly locate gas-liquid and liquid-solid interfaces, as was done for this study.

For all three datasets, an equivalent, generalized data collection methodology was utilized to measure, using Inkscape, liquid separation between

<sup>6</sup>K20  $\rho_L$ -values are obtained using figure 10 of their paper (temperature-dependent correlations for  $\mu_L$  and  $\rho_L$ ); no such correlation is available for  $\sigma$  and thus a singular value is utilized.

<sup>7</sup> $\forall j$ : for all defined values of  $j$ .

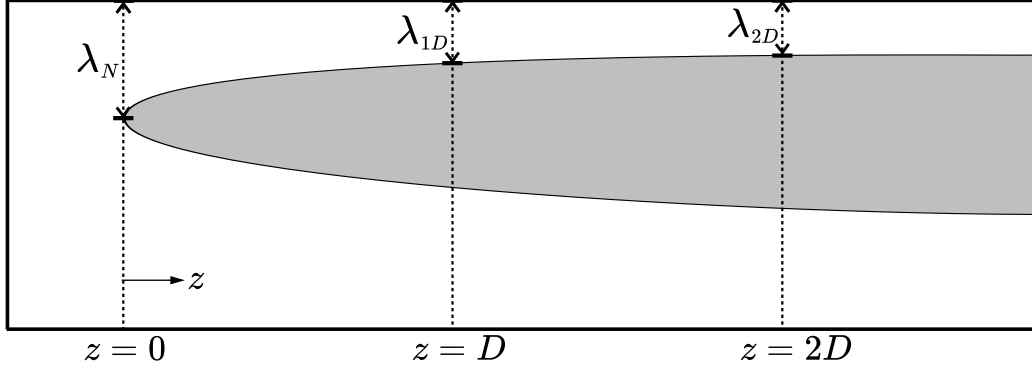


Figure 2: Simplistic depiction of a centred elongated bubble (nose region) in horizontal gas-liquid slug flow overlaid with  $\lambda_N$ ,  $\lambda_{1D}$  and  $\lambda_{2D}$  metrics.

upper pipe wall and elongated bubble top at strategically predefined spatial coordinates. Measurement specifics and data availability vary uniquely between sets, however, as is discussed later in this section. A complete list of obtained metrics is given below wherein “separation” indiscriminately refers to the aforementioned distance between top-of-bubble and upper pipe wall:

- $\lambda_{1D}$ : separation one diameter upstream of bubble nose-tip
- $\lambda_{2D}$ : separation two diameters upstream of bubble nose-tip
- $\lambda_N$ : separation at bubble nose-tip
- $\lambda_B$ : separation at an arbitrary location within bubble body, averaged using three points each spaced apart by one diameter
- $\lambda_T$ : separation at bubble tail—an upstream location at which average bubble body shape deteriorates

Figure 2 provides a visual depiction of  $\lambda_{1D}$ ,  $\lambda_{2D}$  and  $\lambda_N$  whereas  $\lambda_B$  and  $\lambda_T$  are shown in figure 3. Centring- or  $\lambda$ -metrics—meaningless in absolute terms—must be described relative to pipe diameter. Throughout this study they are given in fractional or normalized forms such as

$$\lambda_K^\circ = \frac{\lambda_K}{D} \quad (3)$$

where the index  $K$  represents any of the earlier described subscripts and  $\lambda_K^\circ$  is a percentage. Using the outlined metrics, four types of long bubble centring are formally defined:

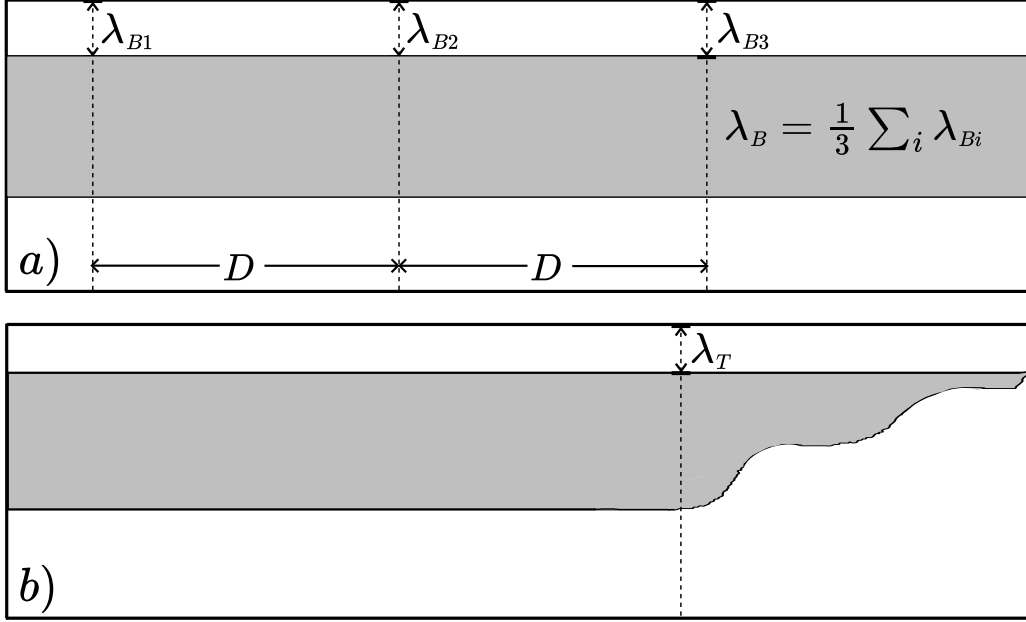


Figure 3: Bubble centring metrics a) in the body  $\lambda_B = \sum_i \lambda_{Bi}/3$  and b) at the tail  $\lambda_T$ .

**No-centring:** null or negligible  $\lambda_{1D}^\circ$

**Partial-centring:** non-negligible  $\lambda_{1D}^\circ$  and null or negligible  $\lambda_T^\circ$

**Full-centring:** non-negligible  $\lambda_{1D}^\circ$ ,  $\lambda_B^\circ$  and  $\lambda_T^\circ$

**Perfect-centring:** non-negligible  $\lambda_{1D}^\circ$ ,  $\lambda_B^\circ$  and  $\lambda_T^\circ$  with equivalent spacing beneath the bubble—radial symmetry<sup>8</sup>

The downstream delimiter is selected to be  $\lambda_{1D}^\circ$ , rather than  $\lambda_N^\circ$ , because the bubble nose-tip is subject to a high level of variability (Diaz, 2016) and, as such,  $\lambda_N^\circ$  could be large while the rest of the bubble remains attached to the upper pipe wall. The concept of perfect-centring is an idealization originally discussed by Bendiksen (1984) wherein the entire bubble flows in complete alignment with the pipe centreline. Partial- and full-centring terminologies were put forth in the PL20 study; the former is commonly

<sup>8</sup>The variable  $\lambda_{1D}^\circ$  alone defines no-centring because centring extent begins at long bubble nose; thus, a flow-case wherein  $\lambda_{1D}^\circ$  is null or negligible while farther upstream locations are detached is non-physical. Partial-centring is classified using  $\lambda_{1D}^\circ$  and  $\lambda_T^\circ$  since it can manifest in a wide range of configurations. Full-centring requires that the entire bubble is centred; however, only when  $\lambda_T^\circ$  is near negligibility must  $\lambda_B^\circ$  also be checked.

observed in air-water slug flow wherein approximately  $1 - 3D$  of the bubble’s nose region is separated from upper pipe wall.<sup>9</sup> Also defined for convenience is a normalized form of liquid viscosity

$$\mu_L^\circ = \frac{\mu_L}{\mu_w} \quad (4)$$

where  $\mu_w = 1\text{mPa s}$  is standard dynamic viscosity of water; therefore,  $\mu_L^\circ = \mu_L$  and units can be dropped.

Not all defined centring metrics can be obtained in every flow-case included here. Regarding the N23 (i.j) dataset,  $\lambda_B$  cannot be determined since bubble body photos are not supplied; however, all other introduced centring metrics are measured. Tail-separation—represented by  $\lambda_T$ —is omitted for cases  $\{2.j \mid \forall j\}$  owing to selective exclusion of tail photos for  $Fr = 1.5$  in the original source. For cases  $\{A.k \cup B.k \mid \forall k\}$  from S24, all five metrics are quantified using available nose, body and tail photos; for case C.1, only  $\lambda_{1D}$ ,  $\lambda_N$  and  $\lambda_T$  can be found due to an atypically short elongated bubble. For K20 cases  $\{\Omega.q \mid \forall q\}$ ,  $\lambda_{1D}$ ,  $\lambda_N$  and  $\lambda_T$  are the only metrics available for extraction. Pairs of  $(Fr, \mu_L)$  are designated in all flow-cases; however, not all cases have obtainable values of  $\gamma$ . Only for cases  $\{1.j \mid \forall j\}$  in N23 can  $\gamma$  be deduced while for S24 and K20, superficial flow ratio is calculable in all cases from m.k and  $\Omega.q$ .

Methodological specifics employed in ascertaining centring data from N23 cases are outlined here; then, notable differences in approach required for S24 and K20 are discussed to follow. The N23 dataset features six  $\mu_L$ -cases at each of  $Fr \in \{1, 1.5, 2, 3, 4\}$  and a liquid viscosity spread of  $\mu_L^\circ \in \{1, 5.5, 10.3, 15.4, 20.3, 30.4\}$ . In their experiments, water served as the non-viscous baseline and differing mixtures of water and glycerin were utilized to concoct higher- $\mu_L$  fluid types. Nose photos from N23—brightened using the “Age” filter in Inkscape—are showcased in figure 4 with corresponding case numbers and  $(Fr, \mu_L)$  pairs. With respect to tail photos, readers are referred to figure 6 of the original study [Naidek et al. \(2023\)](#).

To ensure accurate determination of centring metrics, each photographic data-point was calibrated; namely, the pipe’s fluid-filled internals were distinguished from the upper and lower edges of solid pipe wall. It is assumed that each collection of photos, as originally published, has identically shared

---

<sup>9</sup>The term “fully centred” is used in [Bendiksen \(1984\)](#) but formally defined in PL20.

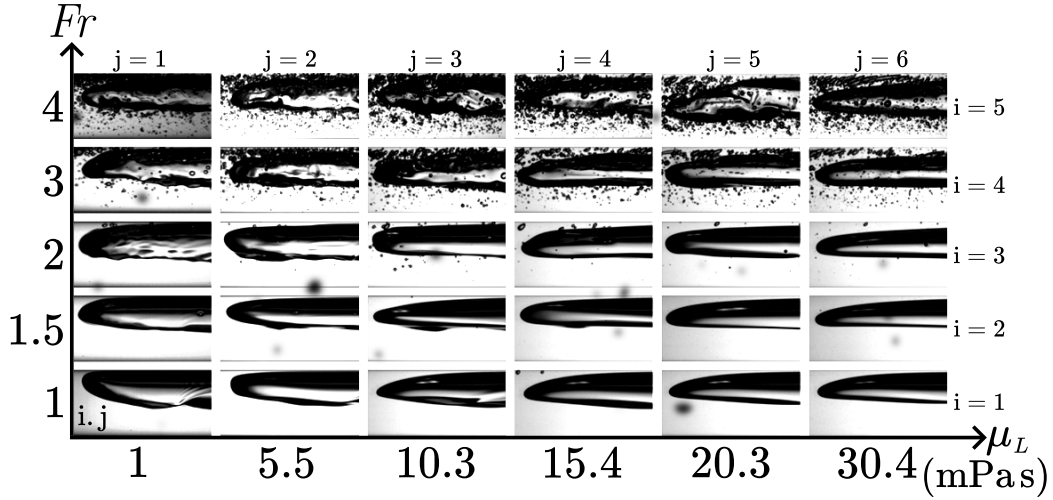


Figure 4: Elongated bubble nose region images from [Naidek et al. \(2023\)](#) (N23 dataset) sorted by mixture Froude number  $Fr$  and liquid viscosity  $\mu_L$ , overlaid with adopted case numbers/set notation  $i.j$ . Adapted from figure 5 of original source with permission from Elsevier Publishing. Photos were brightened/sharpened using Inkscape’s built-in “Age” filter (causing grey “blob” artifacts); otherwise unaltered.

dimensionality, meaning that no geometric alterations were performed that were not implemented for the entire batch. Upon transference of images from source to Inkscape, aspect ratio was retained perfectly; thus, the above assumption permits definition of a constant inner diameter applicable to the entire set, used to normalize centring distances. Regardless, diameter was measured for each photo and an average was taken to negate minor deviations. To do so, image boundaries were inspected at the maximum possible level of magnification (25,600x) and a thin horizontal bar with obviously different pixel density—relative to the pipe interior—was discovered. This artifact is presumed to represent solid pipe; therefore, its interior edge was chosen to mark the boundary of inner pipe diameter, applied to both upper and lower limits. Absolute units of length alluded to here are irrelevant outside of the Inkscape session they were born from, hence the usage of relative metrics which allow scaling to experimental design. Vertical centring distances were collected procedurally using Inkscape’s ruler-tool, performed with meticulous care yet still subject to a small degree of human error. When uncertainty was encountered—for example, in instances where dispersed bubbles obscure

visualization of the gas-liquid interface—a partial-contour was approximately drawn to dictate measurement limits (not shown here).

Also recorded are qualitative measures of interfacial smoothness and small bubble entrainment.<sup>10</sup> Both classifications have three categories: smooth (S), wavy (W) and transitional (T) for the former; non-negligible (Y), near-negligible (N\*) and negligible (N) for the latter. Such distinctions are important—tortuosity along the phasic boundary logically indicates turbulence in the adjacent liquid while significant dispersed bubble content results from large shear forces ripping gas out of its bulk container. Further, interfacial non-smoothness may affect evaluation of centring metrics; for example, a random peak situated at a designated measurement location would lead to a reduced value of reported separation in comparison to immediately neighbouring regions—an outlier. Ideally, an averaged bubble contour would be obtained based on a large number of photos taken at identical operational conditions to reduce the impact of stochastic structuring; however, limited data availability necessitates that singular snapshots are assumed to provide sufficient representations of mean interfacial placement.

The S24 (m.k) dataset features HVL slug flow with two synthetic oil profiles  $\mu_L^\circ \in \{37.7, 352\}$ , both of which are more viscous than any liquid used in N23. Included are two  $Fr$ -values for the lighter oil  $(Fr)_{\mu_L^\circ=37.7} \in \{1.92, 3.23\}$  and three for the heavier oil  $(Fr)_{\mu_L^\circ=352} \in \{0.68, 1.81, 2.94\}$ .<sup>11</sup> Rearranged in contrast to their original publication, raw images are displayed in figure 5. Analyses similar to those described for N23 were performed; however, unlike in N23, long bubble body photos are available and thus values of  $\lambda_B$  were measured using a spatial average as shown in figure 3a. Case C.1 is an anomaly in that a singular photo captures all of nose, body and tail regions. Its unusually short length renders bubble body and tail inseparable; thus, special treatment was implemented. Namely, values of  $\lambda_N$ ,  $\lambda_{1D}$  and  $\lambda_T$  were

---

<sup>10</sup> “Interfacial smoothness” here refers to the long bubble’s lower boundary.

<sup>11</sup>The original S24 paper also includes photographic data featuring plug flow, distinguished from slug flow (figure 8 of source); however, only designated cases of slug flow were utilized for analysis here, primarily because the majority of plug flow cases stem from ultra-low  $Fr$ -values or extremes in  $\gamma$  and an entire study could be devoted to characterizing bubble detachment. Further, bubble shapes are, in many cases, atypical, meaning that metrics such as  $\lambda_T$  would require redefinition. One plug flow case (figure 8d in S24) is an operational counterpart to case C.1 used here; as such, its centring measurements were taken and are mentioned in brevity in §3.1 despite it not being a formal case.

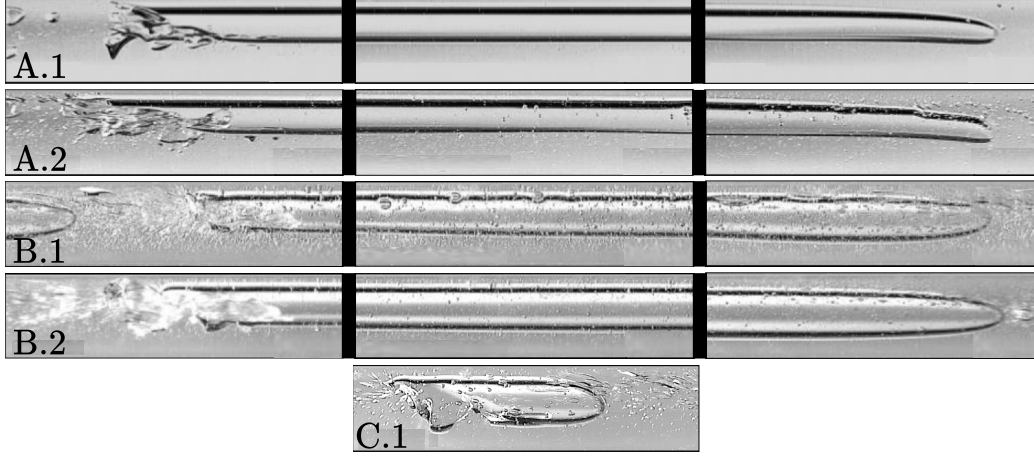


Figure 5: Raw, unaltered images of elongated bubbles from Shin et al. (2024) (S24 dataset) overlaid with case numbers/set notation m.k: bubble nose (right), body (middle) and tail (left) (consolidated for C.1). Case A.1:  $\mu_L = 37.7\text{mPa}\cdot\text{s}$ ;  $Fr = 1.92$ ;  $\gamma = 3.25$ . Case A.2:  $\mu_L = 37.7\text{mPa}\cdot\text{s}$ ;  $Fr = 3.23$ ;  $\gamma = 0.78$ . Case B.1:  $\mu_L = 352\text{mPa}\cdot\text{s}$ ;  $Fr = 1.81$ ;  $\gamma = 3.00$ . Case B.2:  $\mu_L = 352\text{mPa}\cdot\text{s}$ ;  $Fr = 2.94$ ;  $\gamma = 0.59$ . Case C.1:  $\mu_L = 352\text{mPa}\cdot\text{s}$ ;  $Fr = 0.68$ ;  $\gamma = 0.50$ . Black bars separating nose/body/tail photos do not represent scaled length. Adapted from figures 10 and 11b of original source with permission from Elsevier Publishing.

measured normally but—since the tail location is equivalently  $\lambda_{1,34D}—\lambda_{2D}$  does not exist and  $\lambda_B$  cannot be properly measured. As such, the  $\lambda_T$ -value for C.1 is not straightforwardly comparable to those of other cases; regardless, it is kept for completeness. For all other S24 cases  $\{\text{m.k}\backslash\text{C.1}\}$ , the five defined centring metrics were calculated in the above standardized manner.

An additional layer of complexity presented itself in S24 data analyses; namely, the laboratory-specific illumination system evidently creates—in resultant photos—two distinct, differently coloured regions at the long bubble’s upper interface: a thick black line underneath a layer of white. Careful discernment is thus required to accurately determine the top-of-interface, necessitating knowledge of the bubble’s 3-dimensional nature. In N23 data, there is less ambiguity since bubble contours are black and plainly contrasted by the grey surrounding liquid. In S24 flow-cases, however, the bubbles’ global maxima must be selected according to the top of the aforementioned white region since the black line corresponds to a false top localized by the observer/camera. This issue is least apparent in case A.1, plausibly due to a cross-sectionally flat bubble and thus merging of the two regions. Figure 6 offers a simplistic depiction of the optical phenomenon.

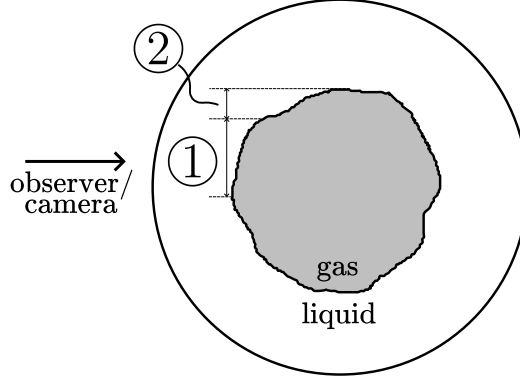


Figure 6: Hypothetical depiction of optical phenomenon observed in [Shin et al. \(2024\)](#) (S24) elongated bubble flow-cases. Region ① is a thick black line that, on first glance, appears to be the top of the gas-liquid interface; however, region ② represents the actual top. Readers are referred to figure 5 for real examples.

Visual data from K20 ( $\Omega.q$ )—simultaneously representing the highest  $\mu_L$ -range  $\mu_L^\circ \in \{510, 680, 960\}$  and lowest inertial supply  $Fr = 0.57$  studied here—were extracted and analyzed using methodology presented above with a few minor logistical deviations. Images were rearranged from their original presentation and are provided here in figure 7 wherein each case is composed of four photographic segments. Black separating bars are designed approximately to-scale at left and right divisions through extrapolation of interfacial evolution; however, since total bubble length is not supplied, middle dividers are non-representative of missing distance. Since required visuality is absent for  $\lambda_{2D}$  and  $\lambda_B$  locations—instead residing somewhere within the middle dividers—only  $\lambda_{1D}$ ,  $\lambda_N$  and  $\lambda_T$  metrics were measured for K20 cases.<sup>12</sup>

## 2.2. Model derivation

Capitalizing on a relatively large sample size, correlative models are construed specifically for N23 data. Derived here, the generalized model outputs centring distances as a function of  $Fr$  and  $\mu_L$ , applicable, at minimum, within the range of pipe, fluid and operational conditions used in the original source. A characteristic dimensionless number is utilized, denoted  $x$  and

<sup>12</sup>Alternative slug flow cases are shown in K20; however, only the three included here are published in raw format—the others utilize a lighting system at the upper pipe wall which renders centring distances undetectable and thus are not used here.

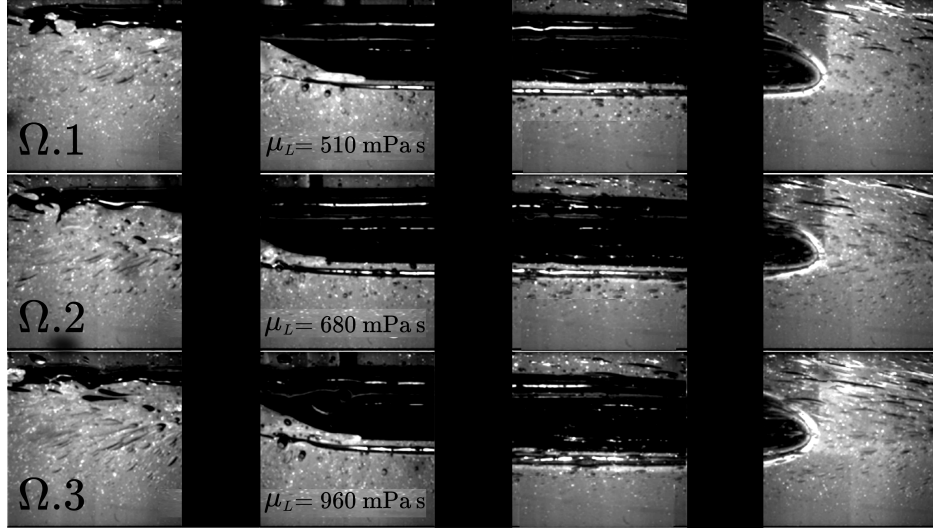


Figure 7: Elongated bubble photos from Kim et al. (2020) (K20 dataset) spliced together to form coherent illustrations. Middle dividers and thus total bubble length are not to-scale; left and right dividers are approximately scaled. Case  $\Omega.1$ :  $\mu_L = 510\text{mPa s}$ . Case  $\Omega.2$ :  $\mu_L = 680\text{mPa s}$ . Case  $\Omega.3$ :  $\mu_L = 960\text{mPa s}$ . For all  $\Omega.q$ ,  $Fr = 0.57$  and  $\gamma = 1.00$ . Adapted from figure 26 of original source with permission from Elsevier Publishing. Photos were brightened/sharpened using Inkscape’s built-in “Age” filter; otherwise unaltered.

defined as

$$x = Fr \frac{\mu_L}{\mu_G} \quad (5)$$

where  $\mu_G$  is gas viscosity—assumed to be  $\mu_G = 0.0181\text{mPa s}$  for air at standard pressure and  $T = 19^\circ\text{C}$ .<sup>13</sup> After some manual exploration, the data were found best fit to a function of the form

$$\lambda^\circ = \Lambda + \Upsilon x + \Theta \ln x \quad (6)$$

where  $\lambda^\circ$  can be  $\lambda_{1D}^\circ$ ,  $\lambda_{2D}^\circ$  or  $\lambda_N^\circ$  and constants  $\Lambda$ ,  $\Upsilon$  and  $\Theta$  are to be calibrated separately for each form of  $\lambda^\circ$ -metric. Inserting 5 into 6 yields

$$\lambda^\circ = \Lambda + \Upsilon Fr \frac{\mu_L}{\mu_G} + \Theta \ln \left( Fr \frac{\mu_L}{\mu_G} \right). \quad (7)$$

<sup>13</sup>Determined using *The Engineering Toolbox* online air viscosity calculator: [https://www.engineeringtoolbox.com/air-absolute-kinematic-viscosity-d\\_601.html](https://www.engineeringtoolbox.com/air-absolute-kinematic-viscosity-d_601.html); accessed 2024-12-07.

Using methodology described in [Chapra \(2012\)](#), least squares regression was employed to optimize equation 7 in correspondence with inferred bubble centring data. The summation of squared residuals is given by

$$S_r = \sum_{n=1}^N (\lambda^\circ - \Lambda - \Upsilon x - \Theta \ln x)^2 \quad (8)$$

where  $N$  is the number of data points used for a given regression. This problem is one of minimization; namely,

$$\min_{\Lambda, \Upsilon, \Theta} S_r \quad (9)$$

must be pursued—done by determining  $\partial S_r / \partial \Lambda$ ,  $\partial S_r / \partial \Upsilon$  and  $\partial S_r / \partial \Theta$  and equating each to zero, yielding a system of equations that is solved in a straightforward manner. Differentiating 8 leads to

$$\frac{\partial S_r}{\partial \Lambda} = -2 \sum_{n=1}^N (\lambda^\circ - \Lambda - \Upsilon x - \Theta \ln x), \quad (10)$$

$$\frac{\partial S_r}{\partial \Upsilon} = -2 \sum_{n=1}^N (x \lambda^\circ - \Lambda x - \Upsilon x^2 - \Theta x \ln x) \quad (11)$$

and

$$\frac{\partial S_r}{\partial \Theta} = -2 \sum_{n=1}^N (\lambda^\circ \ln x - \Lambda \ln x - \Upsilon x \ln x - \Theta \ln^2 x). \quad (12)$$

From these a linearized system is constructed, given in matrix form by

$$\begin{bmatrix} N & \sum x & \sum \ln x \\ \sum x & \sum x^2 & \sum x \ln x \\ \sum \ln x & \sum x \ln x & \sum \ln^2 x \end{bmatrix} \begin{bmatrix} \Lambda \\ \Upsilon \\ \Theta \end{bmatrix} = \begin{bmatrix} \sum \lambda^\circ \\ \sum x \lambda^\circ \\ \sum \lambda^\circ \ln x \end{bmatrix} \quad (13)$$

which is solved to ascertain values of  $\Lambda$ ,  $\Upsilon$  and  $\Theta$  for each form of  $\lambda^\circ$ . Lastly, the coefficient of determination  $R^2$  is calculated as

$$R^2 = 1 - \frac{S_r}{S_\Sigma} \quad (14)$$

where  $S_\Sigma$  is the total summation of squares given by

$$S_\Sigma = \sum_{n=1}^N (\lambda^\circ - \bar{\lambda}^\circ)^2 \quad (15)$$

and  $\overline{\lambda^\circ}$  is the mean value of the chosen version of  $\lambda^\circ$ . Outlined procedure was carried out algorithmically using MATLAB v.R2024a. Owing to limited data availability, correlations were not derived for S24 and K20; thus, the model is readily applicable only for  $\mu_L^\circ \in [1, 30.4]$ . Extrapolation is plausible but further work is required to verify the model’s usefulness (see §3.2) and encapsulate higher- $\mu_L$  liquids. For a mechanistic approach to modelling the bubble centring phenomenon, readers are again referred to the PL20 study.

### 3. Results

#### 3.1. Empirical observation

Overall, measurements taken from N23, S24 and K20 datasets showcase an intriguing interconnection between bubble centring and liquid viscosity in horizontal slug flow.<sup>14</sup> Data from N23 are plotted in two batches of figures: 8, 9 and 10 in this section; B.26, B.27 and B.28 in Appendix B. The former plots relate  $\lambda_{1D}^\circ$ ,  $\lambda_{2D}^\circ$  and  $\lambda_N^\circ$  to  $\mu_L$  for fixed values of  $Fr$ . Using set notation i.j defined in §2.1 wherein fixed i- and j-values correspond to fixed  $Fr$ - and  $\mu_L$ -values, respectively, these plots display the evolution of  $\lambda^\circ$ -metrics for lines of changing j and constant i. Appended plots show the opposite— $\lambda^\circ$ -metrics versus  $Fr$  for fixed levels of  $\mu_L$ ; or, lines of constant j and variable i. Tail-centring ( $\lambda_T^\circ$ ) values from N23 are uniformly either small or null; therefore, they are provided in table 2 using binary designations (i.e., any tail centring or none). For reference, all of the data gathered in this study, along with case-level parameterization, are given in appended table A.6.

Varying levels of non-linear fluctuation are observed in figures 8, 9 and 10; however, in general, there is an obvious tendency for nose-region centring ( $z \in [0, 2D]$ ) to enlarge for increasing  $\mu_L$  and otherwise unchanging dynamic conditions. As originally predicted in PL20, the extent of long bubble centring is a function not only of  $Fr$  and  $\gamma$  but of  $\mu_L$ . It is further deduced that bubble detachment—a flow event defined in PL20 synonymous with the initiation of bubble centring—occurs at lower  $Fr$ -values in HVL-containing slug flows than in comparable air-water systems. At  $Fr = 1$ , for example,  $\lambda_{1D}^\circ$  is near-negligible for  $\mu_L = 1$  yet  $> 7\%$  for  $\mu_L = 30.4$ .

Analyzing the  $\mu_L$ - $\lambda_K$  trends garnered from N23,  $\lambda_{1D}$  and  $\lambda_{2D}$  tell similar stories of different magnitudes—as is intuitively expected;  $\lambda_N$  follows the same

---

<sup>14</sup>Since the three datasets’  $\mu_L$ -ranges do not overlap, the following designations regarding “levels” of HVL may prove useful: N23=low; S24=medium; K20=high.

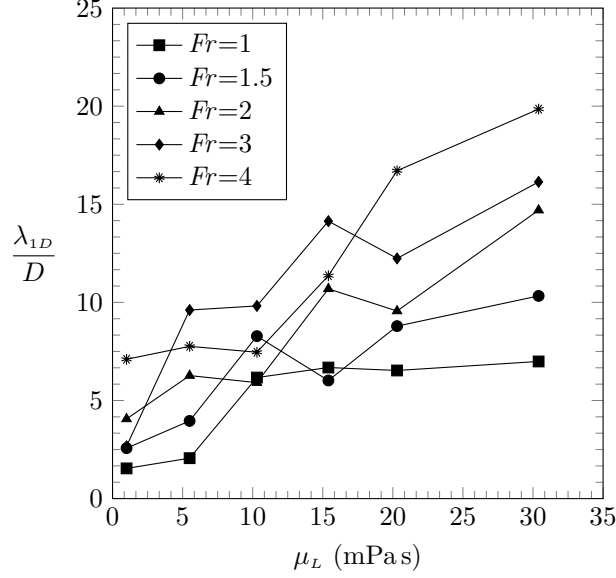


Figure 8: Bubble centring data extracted from [Naidek et al. \(2023\)](#) (N23 dataset): Normalized  $\lambda_{1D}$  (%) as a function of  $\mu_L$  for fixed values of  $Fr$ .

generalized proclivity with a superimposed essence of enhanced variability. To understand this important feature, the undulating nature of the bubble nose must be considered. As an elongated bubble translates in an intermittent configuration, its nose-tip will naturally oscillate in the vertical direction to some extent. This is plausibly due to minor fluctuations in velocity and pressure immediately downstream of the nose-tip effecting radial deviations in the non-rigid long bubble structure. A pictorial example of this phenomenon is found in [Diaz \(2016\)](#) (paper IV; figure 15; single bubble flow experiment with  $\mu_L^\circ = 10$ ) which elucidates the dynamic behaviour of long bubble shape and positioning in horizontal slug flow. For partially- and fully-centred long bubbles, such fluctuations are potentially more pronounced as the nose-tip has additional space to shift. In this context, “fluctuation” could refer to a singular long bubble morphing as it flows or to substantive differences in subsequent long bubble topology and radial placement.

Based on above considerations, the amplified variability observed in N23’s  $\lambda_N$  data (relative to  $\lambda_{1D}$  and  $\lambda_{2D}$ ) is anticipated since measured nose-tip centring evolution stems from arbitrary snapshots rather than averaged contours. In fact, this could account for non-linearity in all three metrics; and,

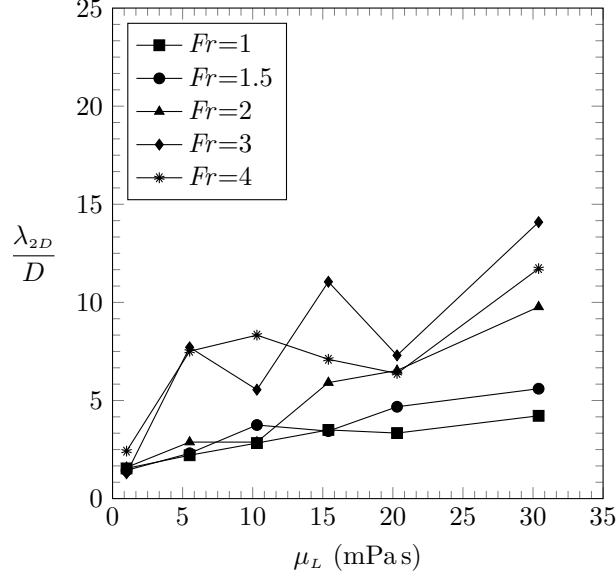


Figure 9: Bubble centring data extracted from [Naidek et al. \(2023\)](#) (N23 dataset): Normalized  $\lambda_{2D}$  (%) as a function of  $\mu_L$  for fixed values of  $Fr$ .

owing to this concept,  $\mu_L$ - $\lambda_K$  curves are expected to flatten somewhat—while maintaining positive proportionality—as centring metric location gets farther from long bubble nose-tip. Referring again to figures 8, 9 and 10, from  $\lambda_N \rightarrow \lambda_{1D}$  linearity is improved in all  $Fr$ -cases; from  $\lambda_{1D} \rightarrow \lambda_{2D}$ , however, curves are flattened for  $Fr \in \{1, 1.5, 2\}$  while non-linearity is roughly preserved for  $Fr \in \{3, 4\}$ . Generally,  $\lambda_{1D}$  and  $\lambda_{2D}$  are deemed reliable indicators of the incurred degree of long bubble centring while  $\lambda_N$  is significantly less relevant due to non-negligible relational volatility. This suggests a paradigmatic change—just as  $\lambda_{1D}$  and  $\lambda_{2D}$  are the empiric centrefold of attention in this study, owing to improved spatial-temporal constancy relative to  $\lambda_N$ , the focus of future experimental works must shift away from an evident exclusivity that places nose-tip position as the ultimate measure of bubble centring extent.

Long bubble tail photos from N23, where available, are assumed to originate from the operational runs of their nose photo counterparts, necessary since their source does not provide  $(u_G^S, u_L^S)$  pairs and instead characterizes

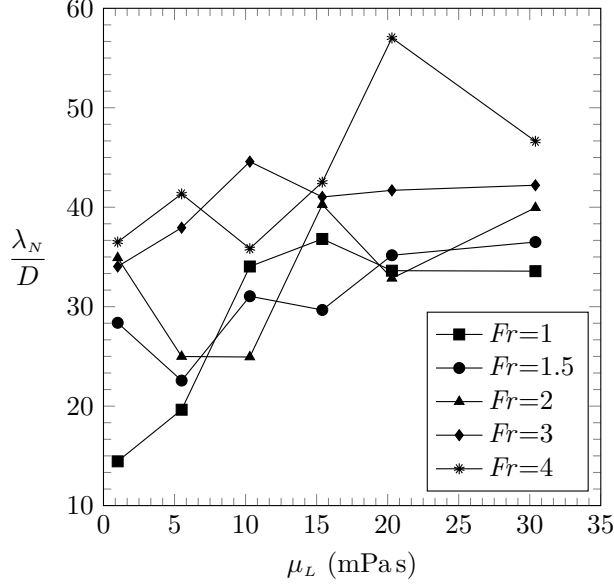


Figure 10: Bubble centring data extracted from Naidek et al. (2023) (N23 dataset): Normalized  $\lambda_N$  (%) as a function of  $\mu_L$  for fixed values of  $Fr$ .

images solely using  $(Fr, \mu_L)$  labels.<sup>15</sup> As alluded to earlier,  $\lambda_T$ -values measured from N23 photos are relatively small, exclusively falling below  $\lambda_T < 0.06D$ ; therefore, tail centring results are visualized in binarized form through table 2 ( $Y \rightarrow$  any amount;  $N \rightarrow$  none). One third of available tail-cases have non-zero  $\lambda_T$ -values (8 of 24); 88% of those are found in either the highest  $Fr$  (5.j) or  $\mu_L$  (i.6) subsets (7 of 8), shown boldfaced in table 2. In fact, the majority of N23’s highest- $Fr$  or - $\mu_L$  cases  $\{5.j \cup i.6\}$  exhibit tail centring (78%; 7 of 9). Centring is characterized here as the existence of non-negligible liquid separation between bubble and upper pipe wall; therefore, a cut-off is required to classify negligible separation, defined here by  $\lambda_K^\circ \leq 2.5\%$ . Using this criterion, 7 of 8 cases with non-zero  $\lambda_T$  show full-centring; and, of 26

<sup>15</sup>This is why  $\gamma$ -values are generally not available for N23 data—superficial flow rate combinations are supplied in a table separate from long bubble photos. For cases  $\{1.j \mid \forall j\}$ , a singular  $(u_G^s, u_L^s)$  pair corresponds to each photographed long bubble; thus  $\gamma$  is known. For  $\{i.j \mid i \geq 3, \forall j\}$ , however, multiple possible  $(u_G^s, u_L^s)$  pairs can be constructed for each long bubble flow-case; hence,  $\gamma$  is unknown. As mentioned in §2.1, tail photos are not available for  $\{2.j \mid \forall j\}$ .

	1	2	3	4	5	6
5	N (PC)	<b>Y</b> (FC)	<b>Y</b> (FC)	<b>Y</b> (FC)	<b>Y</b> (FC)	<b>Y</b> (FC)
4	N (PC)	N (PC)	N (PC)	N (PC)	N (PC)	N (PC)
3	N (PC)	N (PC)	Y (FC)	N (PC)	N (PC)	<b>Y</b> (FC)
2	-	-	-	-	-	-
1	N (NC)	N (NC)	N (PC)	N (PC)	N (PC)	<b>Y*</b> (PC)

Table 2: Extracted tail-centring data for [Naidek et al. \(2023\)](#) (N23) i,j cases. Left-most column: i-values; upper-most row: j-values. Y—tail-centring occurred; Y\*—tail-centring  $< 2.5\%$ ; N—no tail-centring. Bold Y-values correspond to either highest- $Fr$  (5,j) or highest- $\mu_L$  (i,6) subsets. All values observed to be  $\lambda_T < 0.06D$ ; numeric results found in [Appendix A](#). Shown in brackets are centring types as defined in [§2.1](#), determined using a 2.5% cut-off. Since body photos are unavailable, FC cases are assumed to have  $\lambda_B^\circ > 2.5\%$ .

total cases, 15 or 59% are partially-centred by definition (3 water-based; 12 HVL—at least one for each  $\mu_L$ -level). Centring types—as given in [§2.1](#) (FC: full-centring; PC: partial-centring; NC: no-centring)—are also given in [table 2](#) (bracketed) for all N23 cases, determined using the 2.5% distinction.

Shifting focus from low- to medium-HVL designations, long bubble centring data extracted from the S24 (m.k) dataset expands the picture painted by N23 data. Shown in [figure 11](#), all five presently defined centring metrics— $\lambda_{1D}$ ,  $\lambda_{2D}$ ,  $\lambda_N$ ,  $\lambda_B$  and  $\lambda_T$ —are visualized in bar-chart format for cases  $\{\text{m.k} \setminus \text{C.1}\}$ . Due to anomalous features, case C.1 is treated in isolation. Internally comparable case-pairs are construed here to demonstrate the impact of  $\mu_L$  on centring extent; namely,  $\{\text{A.1}, \text{B.1}\}$  and  $\{\text{A.2}, \text{B.2}\}$  represent  $\mu_L$ -contrasted groupings with similar albeit non-identical underlying operational conditions:

$$\text{A.1: } (Fr, \mu_L^\circ, \gamma) = (1.92, 37.7, 3.25)$$

$$\text{B.1: } (Fr, \mu_L^\circ, \gamma) = (1.81, 352, 3.00)$$

$$\text{A.2: } (Fr, \mu_L^\circ, \gamma) = (3.23, 37.7, 0.78)$$

$$\text{B.2: } (Fr, \mu_L^\circ, \gamma) = (2.94, 352, 0.59)$$

Under this logic, [figure 11](#) is designed to elucidate changes in centring distances due primarily to  $(\Delta\mu_L^\circ)_{AB} = 314.3$  in that  $\{\text{A.1}, \text{B.1}\}$  and  $\{\text{A.2}, \text{B.2}\}$  pairs are arranged in juxtaposition and overlaid with %-difference values  $(2\Delta\lambda_K/\Sigma\lambda_K)$  calculated from  $\text{A.k} \rightarrow \text{B.k}$  for each measured centring metric. As was generally observed in N23 analyses, S24 data show that—for otherwise comparable slug flow systems—increasing  $\mu_L$  results in significantly amplified

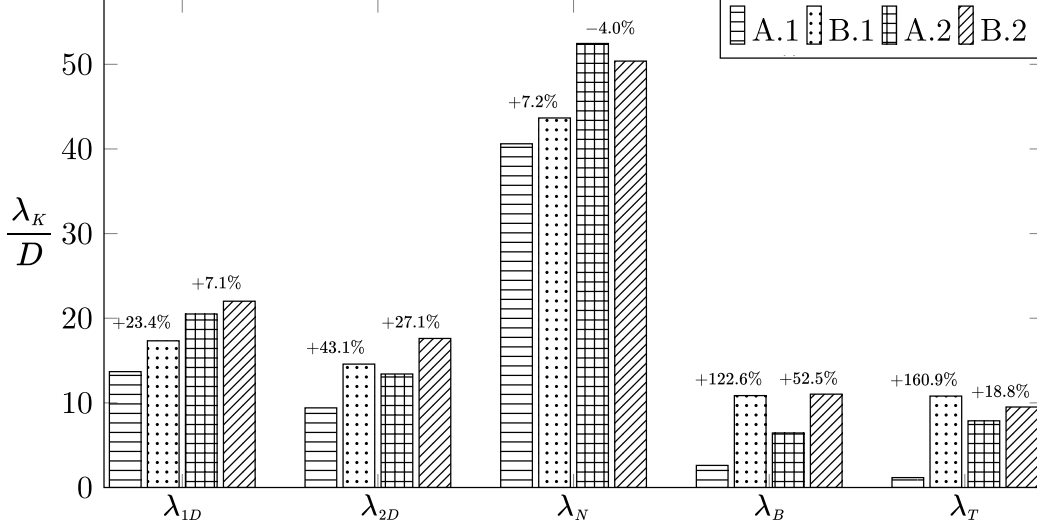


Figure 11: Long bubble centring data extracted from [Shin et al. \(2024\)](#) (S24) m.k cases. All  $\lambda$ -values are normalized by  $D$  and given as a percentage. Overlaid are %-differences between comparable case-pairs  $\{A.1, B.1\}$  and  $\{A.2, B.2\}$  which represent changes in bubble centring extent due to  $(\Delta\mu_L)_{AB} = 314.3\text{mPa.s}$ .

long bubble centring tendencies. A near-perfect positive proportionality is found—all of  $\lambda_{1D}$ ,  $\lambda_{2D}$ ,  $\lambda_B$  and  $\lambda_T$  increase non-negligibly within case-pairs  $\{A.1, B.1\}$  and  $\{A.2, B.2\}$ , especially so in the former at body and tail locations wherein +122.6% and +160.0% differences are seen, respectively. The only exception lies in  $\lambda_N$  measurements. From  $A.1 \rightarrow B.1$ ,  $\lambda_N$  incurs a +7.2% difference; however, from  $A.2 \rightarrow B.2$ , a -4.0% difference is found. This is clearly a stochastic artifact stemming from the long bubble nose-tip's susceptibility to flow-induced oscillation—established earlier in this section. Observing that A.2 and B.2 have  $\lambda_N$ -values near  $0.5D$ —the theoretical limit for bubble centring—the discrepancy becomes explicable due to undulations of the nose-tip about the pipe's centreline and thus noncontradictory to the overall derived relationality between  $\mu_L$  and centring extent.

Centring measurements for S24's case C.1 are given by  $(\lambda_{1D}^\circ, \lambda_N^\circ, \lambda_T^\circ) = (11.9, 43.9, 11.8)\%$ . For reasons described in §2.1, these values are not straightforwardly compared to those obtained for A.k and B.k cases; for example, 12% tail-centring does not indicate that all system-specific slug flows at  $Fr = 0.68$  will experience the same because  $\lambda_T = \lambda_{1.34D}$  for C.1. Since  $\gamma = 0.5$  or, equivalently,  $u_G^S = 0.5u_L^S$ , increasing gas supply while holding  $Fr$

constant—thus reducing liquid supply—may result in a far longer bubble and, by extension, an altered tail-centring profile.<sup>16</sup> Regardless, the case serves as an intriguing theoretical quandary, demonstrating that full-centring can occur in HVL slug flows with extremely low inertial input. For reference, full-centring in air-water flows is associated with  $Fr \geq 3.5$  (Bendiksen, 1984) while initial detachment is found approximately within  $2.2 \leq Fr \leq 2.4$  as interpreted using experiment (de Oliveira et al., 2015) and modelling efforts (Perkins and Li, 2020). That full-centring realization is possible for diminutive operational flow rates is a remarkable feature of high- $\mu_L$  horizontal slug flow, one that solidifies a novel empirical precedent in the widening mechanistic differential between HVL- and water-based systems.<sup>17</sup>

Regarding centring-type designation for other S24 data, 3 of 4 flow-cases  $\{A.k \cup B.k \setminus A.1\}$  exhibit full-centring in compliance with the 2.5% negligibility threshold. Only for A.1—the lowest  $Fr$ -valued run for  $\mu_L^\circ = 37.7$ —was the cut-off invoked since  $\lambda_T^\circ = 2.64\%$  and  $\lambda_B^\circ = 1.17\%$ . A useful metric which gauges the uniformity of incurred centring is  $\lambda_T^\circ/\lambda_{1D}^\circ$  in that  $\lambda_T^\circ/\lambda_{1D}^\circ \rightarrow 1$  suggests equidistant centring throughout the entire long bubble while  $\lambda_T^\circ/\lambda_{1D}^\circ \rightarrow 0$  represents the edge-case of partial-centring. For S24 cases,  $\lambda_T^\circ/\lambda_{1D}^\circ$  values of 0.09, 0.62, 0.38 and 0.43 are found for cases A.1, B.1, A.2 and B.2, respectively, numerics which yet again increase within comparable case-pairs and thus as a positive function of  $\mu_L$ . For pairs of constant  $\mu_L$  and increasing  $Fr$ , however, A.1  $\rightarrow$  A.2 shows an increase in  $\lambda_T^\circ/\lambda_{1D}^\circ$  while B.1  $\rightarrow$  B.2 shows a marked decrease. Intriguingly, while  $(\lambda_{1D}^\circ)_{B.2} > (\lambda_{1D}^\circ)_{B.1}$ , it also holds true that  $(\lambda_T^\circ)_{B.2} < (\lambda_T^\circ)_{B.1}$ , meaning that the nose-extent of centring in B.2—the higher- $Fr$  case—is larger but the evenness of centring is enhanced in B.1. Both B.k cases tend toward perfect-centring realization (see §2.1), more so, in fact, than

<sup>16</sup>Confirmation of C.2’s outlier status is found by comparing its  $\lambda_{1D}$ - and  $\lambda_T$ -values to those from B.k cases (which share  $\mu_L^\circ = 352$ ); namely  $(\lambda_{1D})_{C.1} < (\lambda_{1D})_{B.k}$  and  $(\lambda_T)_{C.1} > (\lambda_T)_{B.k}$  for all k. Since  $(Fr)_{C.1} < (Fr)_{B.k}$ , the former is expected and the latter is not, thus confirming that  $\lambda_T$ -values cannot be compared and C.1 is indeed exceptional.

<sup>17</sup>The lighter-oil plug flow analog to case C.1—mentioned in a §2.1 footnote (p.14) and found in figure 8d of S24’s original paper—is not formally included here; regardless, its centring metrics are given as follows:  $\lambda_{1D}^\circ = 6.60\%$ ,  $\lambda_{2D}^\circ = 5.10\%$ ,  $\lambda_N^\circ = 35.29\%$ , and  $\lambda_T^\circ = 4.68\%$  where  $\lambda_T = \lambda_{3.72D}$ . Compared with C.1, a significant generalized increase in centring is incurred due to  $(\Delta\mu_L)_{AB}$ . Using the 2.5% negligibility criterion, the plug flow case demonstrates full-centring, suggesting that low- $Fr$  tendencies displayed by C.1 hold true also for the lighter-oil (although case A.1 shows partial-centring). For reference, the case in question is derived from  $Fr = 0.72$ ,  $\gamma = 0.6$  and  $\mu_L^\circ = 37.7$ .

any others studied here. For example, case B.2 shows 22.01% detachment at  $z = D$  while, at the same location, the bubble occupies 54.8% of inner pipe height—this leaves 23.2% or  $0.232D$  underneath the bubble, meaning that  $\lambda_{1D}^\circ$  is merely 0.6% less than conditions resembling near-nose perfect symmetry. At the bubble tail, there is 11.03% detachment and a bubble height of 54.2%, yielding a space of 34.8% or  $0.348D$  beneath; thus, if  $\lambda_T^\circ$  were increased 11.9% in this case, perfect symmetry would be approximately realized for the entirety of the film region.<sup>18</sup>

Another notable observation—not as clearly seen in N23 data—is garnered from the S24 dataset; namely, increasing  $\mu_L$  drastically impacts elongated bubble shape, particularly at the nose region. In the lighter-oil cases  $\{\text{A.k} \mid \forall k\}$ , the bubble nose is thin and markedly curved toward the downward direction, resulting in plainly visible asymmetry; in the heavier-oil cases  $\{\text{B.k} \mid \forall k\}$ , however, the bubble nose is thick and symmetrical, especially in the higher- $Fr$  version B.2 wherein perfect-centring is nearly realized for at least  $4D$  from nose-tip, as discussed above. Within comparable case-pairs  $\{\text{A.1}, \text{B.1}\}$  and  $\{\text{A.2}, \text{B.2}\}$ ,  $Fr$  and  $\gamma$  are numerically similar—since roughly equal volumes of gas and liquid are supplied amidst pairings, it is evident that  $(\Delta\mu_L)_{AB}$  alters the 3-dimensional distribution of phases. S24’s authors mention that higher- $\mu_L$  results in curtailing of bubble length. For the lighter-oil cases, gas is stretched over a longer distance and thus thinner—viewed perpendicularly to flow—than in the heavier-oil cases. Improvement in axial symmetry signifies greater coherence of centring mechanisms or downward suction applied to the bubble. That such an enhancement is correlated with increasing  $\mu_L$  is conducive to the overall narrative derived here. To further comprehend the impact of  $\mu_L$  on long bubble shape and centring manifestation, cross-sectional photos—obtained using specialized experimental design such as that utilized in [Jamari et al. \(2008\)](#)—are necessary.

Bubble centring measurements extracted from K20—representing the highest range of  $\mu_L$ -values studied here with  $\mu_L^\circ \in \{510, 680, 960\}$ —are shown in figure 12 using bar-chart formatting. All three  $\Omega.q$  cases feature equivalent operational conditions:  $(Fr, \gamma, D) = (0.57, 1, 50.8\text{mm})$ . Since non-negligible  $\lambda_T$ -values are measured in each, these flow-cases remarkably exemplify the

---

<sup>18</sup>However, a peculiar observation arises in comparing body- to tail-centring for S24 cases:  $\lambda_B^\circ < \lambda_T^\circ$  for  $\{\text{A.1}, \text{B.2}\}$ ;  $\lambda_B^\circ \approx \lambda_T^\circ$  for B.1; and,  $\lambda_B^\circ > \lambda_T^\circ$  for A.2. This suggests that  $\lambda_T^\circ/\lambda_{1D}^\circ$  is only a rough measure of centring evenness in that separation distances do not always decrease linearly from nose-tip to tail.

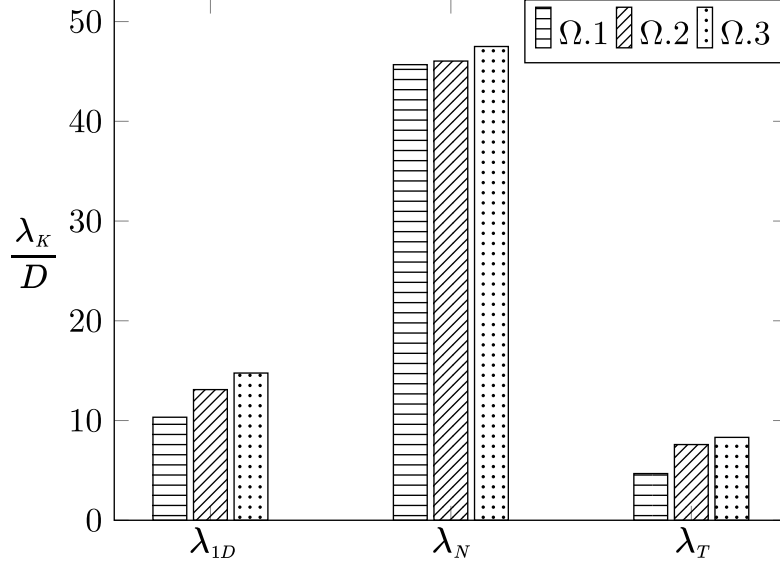


Figure 12: Long bubble centring data extracted from Kim et al. (2020) (K20)  $\Omega.q$  cases. All  $\lambda$ -values are normalized by  $D$  and given as a percentage. Here,  $\mu_L \uparrow$  as  $q \uparrow$ .

tendency of HVL slug flow systems to exhibit full-centring under relatively low inertial input. As in S24’s C.1,  $\Omega.q$  cases display complete detachment from the upper pipe wall for  $Fr < 0.7$ , indicated by a thin liquid film above the elongated bubble which thickens with increasing  $\mu_L$ . Unlike C.1, however, K20 cases are observed with relatively normal bubble lengths, rendering them non-anomalous and thus stronger examples of the aforementioned low- $Fr$  tendency in HVL flows. As outlined in §2.1, only  $\lambda_{1D}$ ,  $\lambda_N$  and  $\lambda_T$  centring metrics are available for K20 flow-cases; for all three, a positive change is incurred across each of the incremental  $\mu_L$ -increases:  $(\Delta\mu_L^\circ)_{12} = 170$  from  $\Omega.1 \rightarrow \Omega.2$  (+28.6%) and  $(\Delta\mu_L^\circ)_{23} = 280$  from  $\Omega.2 \rightarrow \Omega.3$  (+34.1%). Table 3 provides %-difference values—both for the two aforementioned  $\mu_L$ -shifts and for total change:  $(\Delta\mu_L^\circ)_{13} = 450$  from  $\Omega.1 \rightarrow \Omega.3$  (+61.2%). The largest step-wise differences are seen in  $\lambda_T$  and  $\lambda_{1D}$  for  $\Omega.1 \rightarrow \Omega.2$  with +47.4% and +23.7%, respectively, while the smallest differences are observed in  $\lambda_N$  with  $\leq +3.1\%$  for both  $\mu_L$ -shifts.

As mentioned, all three K20 cases exhibit full-centring under the  $\lambda_K^\circ > 2.5\%$  negligibility cut-off. The generalized extent of centring is significantly less in  $\{\Omega.q \mid \forall q\}$  than in S24’s  $\{B.k \mid \forall k\}$  cases as evidenced by  $\lambda_{1D}^\circ$  and  $\lambda_T^\circ$  measurements; however, this is expected owing to the rather low  $Fr$ -value

	$\mu_L$	$\lambda_{1D}$	$\lambda_N$	$\lambda_T$
$\Omega.1 \rightarrow \Omega.2$	+28.6	+23.7	+0.8	+47.4
$\Omega.2 \rightarrow \Omega.3$	+34.1	+11.9	+3.1	+9.0
$\Omega.1 \rightarrow \Omega.3$	+61.2	+35.4	+3.9	+55.8

Table 3: %-difference values for [Kim et al. \(2020\)](#) (K20) bubble centring measurements, representative of changes induced by corresponding  $\Delta\mu_L$ .  $\Omega.1 \rightarrow \Omega.2$ :  $(\Delta\mu_L)_{12} = 170\text{mPa}$ s;  $\Omega.2 \rightarrow \Omega.3$ :  $(\Delta\mu_L)_{23} = 280\text{mPa}$ s;  $\Omega.1 \rightarrow \Omega.3$ :  $(\Delta\mu_L)_{13} = 450\text{mPa}$ s. Values given in %, calculated using standard  $2\Delta\lambda_K/\Sigma\lambda_K$  or  $2\Delta\mu_L/\Sigma\mu_L$ .

used in available K20 flow-cases. Values of  $\lambda_T^\circ/\lambda_{1D}^\circ$ —a metric indicative of centring evenness discussed earlier—are calculated to be 0.45, 0.58 and 0.56 for cases  $\Omega.1$ ,  $\Omega.2$  and  $\Omega.3$ , respectively, suggesting relatively coherent uniformity of centring in all instances. Across  $(\Delta\mu_L^\circ)_{12}$ , an increase in  $\lambda_T^\circ/\lambda_{1D}^\circ$  is incurred (+24.4%); across  $(\Delta\mu_L^\circ)_{23}$ , however, a near-negligible decrease is observed (−2.9%), suggesting that approximate centring evenness stabilizes for  $\mu_L^\circ \geq 680$  in the system of interest.<sup>19</sup>

Next, the continuity of utilized datasets is investigated. In this context, “continuity” is the potentiality for seamless extrapolation of data-based trends between differing sources. Were it not established, a question would be aroused as to whether empirically derived conclusions stem from an irreproducible environment—possibly due to a group-dependent method or parameter—thus making inter-laboratory integration unfeasible. Certain differences between N23, S24 and K20 datasets must first be clarified; for example, all were born using different pipe sizes. N23 and S24 are most similar in this regard with a 26.1% difference; with respect to K20, there are 87.0% and 64.6% differences in contrast with N23 and S24 pipe diameters, respectively. Another notable discrepancy is utilized fluid type: N23 used water-glycerin mixtures while both S24 and K20 used various synthetic oils, all with differing values of liquid density  $\rho_L$  and surface tension  $\sigma$ , as reported in §2.1. The role of non- $\mu_L$  fluid property diversity in bubble centring realization is yet to be studied

<sup>19</sup>Also worth noting is that all three K20 flow-cases feature a smooth gas-liquid interface, indicative of laminarity in the liquid film. The same is observed in S24 cases; however, in A.2 and B.1 there are minor non-linearities on the upper (near-nose) bubble boundary. A variety of interfacial classifications are found in N23 cases. As will be seen in §4.1, such conditions are important considerations in the initiation of bubble centring.

in-depth; however, increasing  $\rho_L$  is intuitively counterproductive to centring as a denser liquid is more inclined to remain underneath the long bubble owing to gravity's pull. The extent of this effect for incremental changes in  $\rho_L$  is unclear, as is the impact of differing  $\sigma$ . Despite these unknowns and significant differences in non- $\mu_L$  liquid properties, it is assumed that N23 & S24 form an optimal pair for probing empiric continuity, given their similar values of  $D$ . K20 is ignored in this endeavour due to its non-conforming pipe size and uniformly low values of  $Fr$ , in that the majority of N23/S24 cases do not have similar  $Fr$ -cases in K20 to be compared with.

Judging by case-level contrasting, the culminated results of N23 and S24 bubble centring inquiry craft a tapestry of robust connectivity. For example, A.1 of S24 is best compared to N23's cases 2.6 and 3.6: A.1 features  $(Fr, \mu_L^\circ) = (1.92, 37.7)$  while 2.6 and 3.6 are characterized by  $(Fr, \mu_L^\circ) = (1.5, 30.4)$  and  $(Fr, \mu_L^\circ) = (2.0, 30.4)$ , respectively, meaning that  $(Fr)_{2.6} < (Fr)_{A.1} < (Fr)_{3.6}$  and  $(\mu_L^\circ)_{A.1} > (\mu_L^\circ)_{2.6/3.6}$ —the latter representing a difference of  $\Delta\mu_L^\circ = 7.3$  or 21.4%. Centring analyses for A.1 show that  $(\lambda_{1D}^\circ, \lambda_{2D}^\circ) = (13.69, 9.41)\%$  whereas  $(\lambda_{1D}^\circ, \lambda_{2D}^\circ) = (10.33, 5.60)\%$  and  $(\lambda_{1D}^\circ, \lambda_{2D}^\circ) = (14.70, 9.77)\%$  are obtained for 2.6 and 3.6, respectively. Thus it stands that

$$(\lambda_{1D}^\circ)_{2.6} < (\lambda_{1D}^\circ)_{A.1} < (\lambda_{1D}^\circ)_{3.6} \quad (16)$$

and

$$(\lambda_{2D}^\circ)_{2.6} < (\lambda_{2D}^\circ)_{A.1} < (\lambda_{2D}^\circ)_{3.6} \quad (17)$$

wherein the A.1 centring profile is far more similar to that of 3.6 than of 2.6. The above outcomes are reasonably aligned with continuity in consideration of the three cases'  $Fr$ -inequality and comparable  $\mu_L$ -valuation. S24's higher- $\mu_L$  cases B.1 ( $Fr = 1.81$ ) and B.2 ( $Fr = 2.94$ )—both featuring  $\mu_L^\circ = 352$ —are logically compared to N23's 3.6 ( $Fr = 2$ ) and 4.6 ( $Fr = 3$ ) which utilize  $\mu_L^\circ = 30.4$  ( $\Delta\mu_L^\circ = 321.6$  or 168.2% difference). Centring measurements reveal that

$$\begin{aligned} (\lambda_{1D}^\circ)_{B.1} &> (\lambda_{1D}^\circ)_{3.6} \\ (\lambda_{2D}^\circ)_{B.1} &> (\lambda_{2D}^\circ)_{3.6} \end{aligned} \quad (18)$$

and

$$\begin{aligned} (\lambda_{1D}^\circ)_{B.2} &> (\lambda_{1D}^\circ)_{4.6} \\ (\lambda_{2D}^\circ)_{B.2} &> (\lambda_{2D}^\circ)_{4.6} \end{aligned} \quad (19)$$

which is expected—considering the correlative framework presented thus far—because  $(\mu_L)_{B,k} \gg (\mu_L)_{i,6}$ . In fact, exhaustive data analyses for sets i.j and m.k demonstrate that

$$\max_{i,j,m,k} (\lambda_{1D}^\circ) = (\lambda_{1D}^\circ)_{B,2} \quad (20)$$

and

$$\max_{i,j,m,k} (\lambda_{2D}^\circ) = (\lambda_{2D}^\circ)_{B,2}; \quad (21)$$

meaning, maximal values of  $\lambda_{1D}^\circ$  and  $\lambda_{2D}^\circ$  are encountered in the case of globally maximized  $\mu_L$  (keeping in mind that K20 is not included at present). Furthermore, excluding anomalous case C.1, it holds true that

$$\max_{i,j,m,k \setminus C.1} (\lambda_T^\circ) = (\lambda_T^\circ)_{B,2}. \quad (22)$$

Regardless of systemic differences, relationality derived above suggests that an acceptable level of continuity exists between N23 and S24 datasets. Therefore, the generalized conclusions discovered here are readily extrapolated to other HVL-containing systems; namely, increasing  $\mu_L$  enlarges the probabilistic likelihood and extent of long bubble centring in horizontal slug flow. This investigation, however, although thorough, is preliminary—additional work is required to understand the correlative role of  $\gamma$ , for example, a crucial ratio which is missing for the majority of N23 cases.

An illuminating consequence arises from the established continuity between N23 and S24 datasets: their combined tail-centring results yield insight into a critical  $\mu_L$ -value above which full-centring is anticipated for a broad range of  $Fr$ -values. For N23 data, a maximum of  $\lambda_T^\circ = 6\%$  is obtained; regarding S24's  $\{m.k \setminus C.1\}$ , however, 75% of cases have  $\lambda_T^\circ > 6\%$  and 50% have  $\lambda_T^\circ > 10\%$ , the latter of which stem exclusively from the larger  $\mu_L$  subset. Therefore, a conservative cut-off for statistically likely full-centring occurrence is  $\mu_L^\circ \geq 352$  while the actual boundary lies within  $37.7 < \mu_L^\circ < 352$  as gleamed from the evident blossoming of tail-centring seen at  $\mu_L^\circ = 37.7$ . Considerable further inquiry is necessary to truly affirm this delineation; however, given the contextual structure outlined here, the aforementioned range serves as an adequate heuristic approximation.

Overall, data extraction and analyses delved into here serve as a testament of correlative potential, demonstrating straightforwardly that increasing liquid viscosity has an expanding impact on elongated bubble centring in horizontal gas-liquid slug flow. For reference, all discussed results and parameters are found in [Appendix A](#).

### 3.2. Correlational analysis

Presented in §2.2, an empirical model—described by equation 7—was calibrated using least squares regression to fit N23 bubble centring data, specifically for  $\lambda_{1D}^\circ$ ,  $\lambda_{2D}^\circ$  and  $\lambda_N^\circ$ . Derived coefficients and  $R^2$  values are included in table 4. The most successful global match is obtained for  $\lambda_{1D}^\circ$  with  $R^2 = 0.879$ . Acceptable conformance is found also for  $\lambda_{2D}^\circ$  for which  $R^2 = 0.739$  is calculated, while the least adequate fit is observed for the nose-tip metric  $\lambda_N^\circ$  with  $R^2 = 0.519$ . The latter finding aligns ideologically with discussion provided in §3.1 regarding dynamic variability of the long bubble nose-tip; namely,  $\lambda_N$  is the least reliable metric used here for gauging the extent of centring incurred during slug flow.

	$\Lambda$	$\Upsilon$	$\Theta$	$R^2$
$\lambda_{1D}^\circ$	-1.844	0.00194	1.005	0.879
$\lambda_{2D}^\circ$	-2.497	0.00120	0.820	0.739
$\lambda_N^\circ$	15.106	0.00217	2.343	0.519

Table 4: Results of least squares regression applied to bubble centring data from Naidek et al. (2023) (N23) dataset, as per equation 7.

Figure 13 shows the three derived empirical models overlaid with measured  $\lambda_{1D}^\circ$ ,  $\lambda_{2D}^\circ$  and  $\lambda_N^\circ$  data from N23. Defined in §2.2, the independent variable used is  $x = Fr\mu_L/\mu_G$ , representing a coalescence of dynamical influences: mixture inertial input and liquid viscousness, both of which are shown to affect the degree of realized bubble centring in horizontal slug flow systems. The factor of  $\mu_G$  is included for normalization purposes— $\mu_w$  could have been used identically yielding different coefficient values. Referring again to equation 7, that centring metrics can be modelled with reasonable efficacy by a superposition of linear and logarithmic contributions of  $x$  sheds light on future engineering approaches to incorporating the phenomenon into a multiphase pipe flow design protocol. These particular models are limited in scope to  $\mu_L^\circ \in [1, 30.4]$  and  $D = 20\text{mm}$ ; however, rederivation is straightforward assuming that ample system-specific photographic data are available. Also, going forward,  $\gamma$  ought to be merged into the utilized dimensionless group and thus the correlative process.

To understand potential applications of the derived form of bubble centring correlations, a crucial distinction from the aforementioned PL20 study must

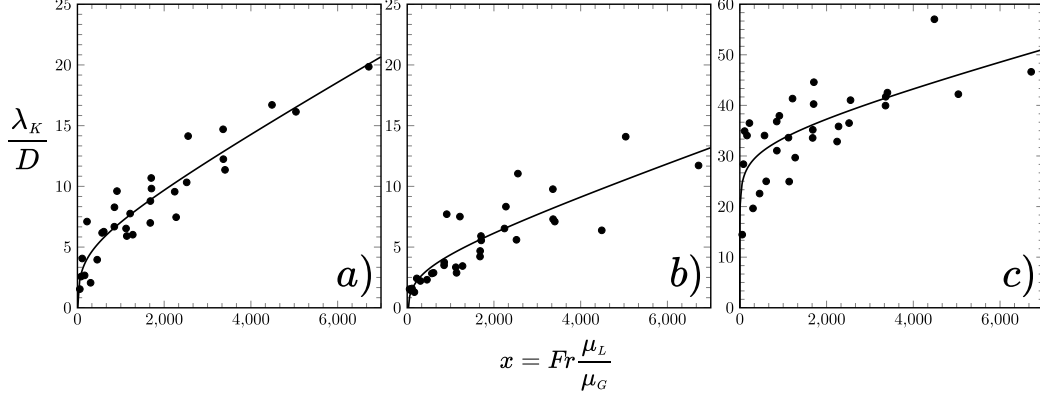


Figure 13: Correlative modelling results for Naidek et al. (2023) (N23) bubble centring data (values given in %):  $\lambda_K^o = \lambda_K/D$  vs  $x = Fr\mu_L/\mu_G$  for a)  $\lambda_{1D}^o$ , b)  $\lambda_{2D}^o$ , and c)  $\lambda_N^o$ . Solid lines: modelling predictions; discrete points: extracted experimental measurements.

be invoked; namely, the difference between detached long bubbles, partial or full, and a thin upper liquid film existing above the non-centred gas phase. In PL20, the latter is deemed a prerequisite for the initiation of the former. If gas alone were in contact with the upper solid wall, the downward force—otherwise causal in detachment—would not be transmitted onto the bubble. This is because a change in vertical pressure differential is required to initiate centring, not simply a change in pressure underneath the bubble. Utilized in §3.1, a threshold value of 2.5% is used to delineate the two unique flow situations.<sup>20</sup> This is summarized as follows:

$$\begin{aligned} \lambda_K^o &> 2.5\%: \text{bubble centring} \\ \lambda_K^o &\leq 2.5\%: \text{thin upper liquid film} \end{aligned}$$

Given a calibrated correlative model constructed using a sufficient amount of bubble centring data, the above cut-off can be utilized to predict the lowest operational rates or  $Fr$ -value at which detachment will occur. Using the modelling structure presented in §2.2, an iterative (or graphical) solution is necessary to calculate the critical value of  $Fr$ . This approach is tested using coefficients determined here. The Newton-Raphson method, as presented

<sup>20</sup>The 2.5% threshold is roughly based on what the naked eye can plainly see as liquid separation in photographic centring data. Values below 2.5% cannot be measured without magnification and careful discernment. Readers are referred again to the PL20 study for a comprehensive discussion of thin upper film phenomena relative to the centring process.

	$\mu_L^\circ$	1	5	10	20	30
$\lambda_{1D}^\circ = 2.5\%$	$(Fr)_D$	1.20	0.24	0.12	0.06	0.04
$\lambda_{2D}^\circ = 2.5\%$	$(Fr)_D$	5.25	1.05	0.52	0.26	0.17

Table 5: Values of detachment Froude number  $(Fr)_D$  predicted by correlative models derived here.  $(Fr)_D$  represents threshold inertial input required to initiate long bubble centring in horizontal slug flow. Delineating separation thickness is defined as  $0.025D$ . Shown for both  $\lambda_{1D}^\circ$  and  $\lambda_{2D}^\circ$  models.

in Chapra (2012), was implemented in MATLAB to solve for detachment Froude number  $(Fr)_D$  corresponding to  $\lambda_{1D}^\circ = 2.5\%$  and  $\lambda_{2D}^\circ = 2.5\%$  at all of  $\mu_L^\circ \in \{1, 5, 10, 20, 30\}$ . Results are presented in table 5.

For a location  $1D$  upstream of long bubble nose-tip, an upper film with  $0.025D$  thickness is predicted at  $(Fr)_D = 1.20$  for air-water slug flow—an underprediction relative to existing literature yet reasonable regardless. For  $\mu_L \in \{5, 10, 20, 30\}$ ,  $(Fr)_D$  calculated based on  $\lambda_{1D}^\circ$  is severely low in that obtained values may not represent physical slug flow solutions. This elicits two possible inferences; namely, the existence of either 1) a critical weakness within the correlative model (e.g., too few input data or a weakly formulated independent variable) or 2) a thin upper liquid film at  $z = D$  by default for the  $\mu_L$ -cases of inquiry, logically maintaining a thickness of  $\lambda_{1D}^\circ > 2.5\%$ . With respect to  $z = 2D$ ,  $(Fr)_D$  is over-predicted for  $\mu_L^\circ = 1$ , reasonably predicted for  $\mu_L^\circ \in \{5, 10\}$  and yet again under-predicted for  $\mu_L^\circ \in \{20, 30\}$ . That calculated  $(Fr)_D$ -values are larger for  $\lambda_{2D}^\circ$  than they are for  $\lambda_{1D}^\circ$  is expected since increased inertial supply is necessary to induce more extensive long bubble detachment (“extent” referring to distance measured upstream from nose-tip). Despite showing promise in regard to outputted order-of-magnitude and underlying relationality, the correlative approach utilized here is a first-order attempt at empirically modelling the bubble centring phenomenon and thus demands further development to become reliably useful.

Finally, figure 14 shows every  $\lambda_{1D}^\circ$ -,  $\lambda_{2D}^\circ$ - and  $\lambda_N^\circ$ -value extracted from N23 flow-cases, both as measured (ordinate) and as predicted by subsequently derived correlative models (abscissa), overlaid with 0%,  $\pm 20\%$  and  $\pm 30\%$  error lines. Of the 90 centring measurements collected, 58.9% and 76.7% are predicted with  $< 20\%$  and  $< 30\%$  error, respectively. Specifically,  $\lambda_{1D}^\circ$  is predicted at 56.7% and 80% accuracy for  $< 20\%$  and  $< 30\%$  error;  $\lambda_{2D}^\circ$

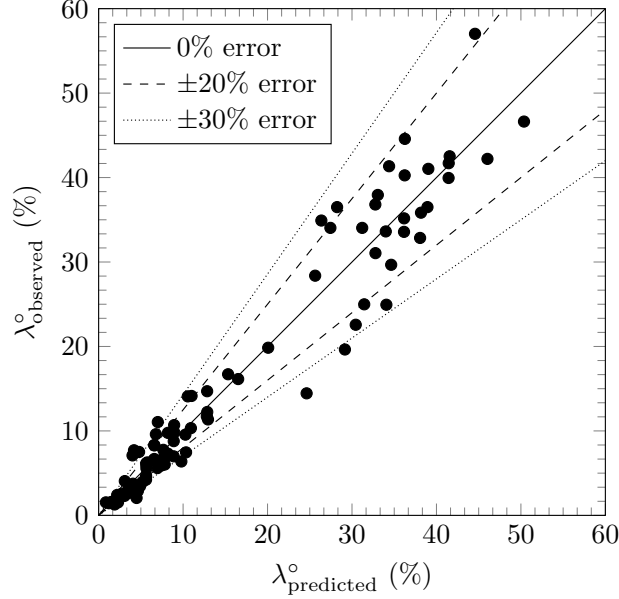


Figure 14: Predicted versus observed values of all  $\lambda_{1D}^\circ$ ,  $\lambda_{2D}^\circ$  and  $\lambda_N^\circ$  bubble centring measurements from Naidek et al. (2023) (N23) dataset overlaid with 0%,  $\pm 20\%$  and  $\pm 30\%$  error lines.

at 46.7% and 63.3%; and  $\lambda_N^\circ$  at 73.3% and 86.7%, respectively. Considering that long bubble centring has a stochastic element, the generalized predictive capacity of empirical models crafted here—when applied to data they were born out of—is deemed satisfactory.

## 4. Theory

### 4.1. Centring mechanics

Having established an unambiguous depiction of correlativity, the governing structure of causality must be investigated. Regarding the flow of gas and liquid in a horizontally-oriented pipe, the presence of an HVL introduces a layer of dynamical complexity not encountered in air-water systems. Postulated here is an understated criticality corresponding to the bubble centring phenomenon, in that it must be afforded careful attention in formulating a theoretical framework which encapsulates the mechanistic workings of HVL slug flow. This notion is empirically founded in §3.1 which demonstrates, in general, that centring distances expand proportionally with

increasing liquid viscosity. The aforementioned PL20 study pioneered a phenomenological explanation for the prevalence of centring in HVL slug flow; namely, film region liquid laminarity—put forth as a condition necessary for long bubble detachment—is probabilistically likely in high- $\mu_L$  flow-systems. Specifically, coherent streamlines—flowing in the upstream ( $+z$ ) direction relative to unit-cell translation—must exist immediately beneath the long bubble for a downward force to be generated. Turbulence can, however, simultaneously endure in other sections of the slug flow architecture; for example, in the mixing region upstream of long bubble tail or adjacent to the film region’s lower pipe wall—the laminarity requirement refers solely to liquid underneath the long bubble.

To better understand the aforementioned streamline concept, the partial-centring configuration must be explored. Air-water and low-HVL slug flows often display partial-centring in that some length of long bubble  $z \in [0, l_D]$  flows detached from upper pipe wall while the remainder  $z \in (l_D, l_B]$  presents in traditional conformation.<sup>21</sup> PL20 describes the existence of a thin upper liquid film (defined numerically in §3.2) as an additional phenomenological prerequisite in the initiation of long bubble centring; axial extent of centring, then, is limited by the sustained extent of thin upper film—represented by  $z = l_{uf}$ . Film region laminarity is taken to be fundamentally true in PL20 analyses and two distinct cases of thin upper film realization are delineated: 1)  $l_{uf} = l_B$  with rigid body mechanics applied to the long bubble such that total pressure differential generates a singular downward force on a non-deformable entity (full-centring or none) and 2)  $l_{uf} < l_B$  under non-rigid bubble dynamics such that downward forces apply only on  $z \in [0, l_{uf}]$  (partial-centring or none). A modified hypothetical approach to characterizing partial-centring is utilized here; namely, granted that a thin upper liquid film stretches over the entire long bubble  $l_{uf} = l_B$ , a regime change partway through the film region acts to modulate partial-centring manifestation.

At this point, it is vital to clarify that liquid velocity distribution in the film region is a predominant driving factor in the production of pressure alterations needed to initiate long bubble detachment in horizontal slug flow. As such, a brief overview of slug flow mechanics is provided here based

---

<sup>21</sup>In conventional literature,  $l_f$  is used to describe film region length; however, following PL20,  $l_B$  is utilized here to denote elongated bubble length. Generally, the two are equivalent:  $l_f = l_B$ .

on the unit-cell assumption—wherein slug and film units flow in sequence with equivalent geometric and dynamic configuration—as per the [Taitel and Barnea \(1990\)](#) (TB90) model.<sup>22</sup> Adhering operational vantage to that of the moving unit-cell—or, equivalently, to elongated bubble translational velocity  $u_t$ —liquid in the film appears, illusorily, to move backward or upstream. A liquid parcel located within the film at  $t_0$  is picked-up by the preceding or upstream slug region at some  $t_1 > t_0$ ; then, the parcel is shed from the slug to be absorbed by the following film region at  $t_2 > t_1$ . This cyclic process unfolds because the unit-cell’s interfacial structure translates faster than all of the present liquid.<sup>23</sup>

As predicted by the TB90 analytical model, absolute velocity of liquid in the film  $u_f$  decreases non-linearly with increasing distance from bubble nose-tip  $z$ .<sup>24</sup> Therefore, relative film velocity  $v_f = u_t - u_f$  increases with  $z$ , leading to the following conclusion in PL20: changes in  $v_f$  across the long bubble’s lower interface create—owing to Bernoulli’s principle—a pressure differential between thin upper film and liquid beneath the gas as mediated by film region laminarity. Since, under the unit-cell simplification, the film region is an inertial or non-accelerating system, a logical argument is made for the potential existence of a dual-regime film configuration: laminarity near-nose and turbulence near-tail, segregated by a transitive spatial marker at which flow forces overwhelm viscous regularity due to increasing relative motion  $\Delta v_f$ . This is analogous to transitional distance beyond the inlet of single-phase pipe flow. Considering context outlined above, this concept—demonstrated visually in figure 15—is hypothesized here to hold a causal role in the realization of partial-centring.

Summarizing figure 15, the defined streamline assumption remains valid for a distance  $l_{st}$  from bubble nose-tip; beyond that, due to a critical relative velocity being reached, it disintegrates as smooth flow trajectories morph into diffusive chaos. As such, only for  $z \in [0, l_{st}]$  can centring mechanisms be applied; and, plausibly, the transitional location marks also the length of

---

<sup>22</sup>TB90: [Taitel and Barnea \(1990\)](#) unit-cell slug flow model. Note that TB90 did not cover or incorporate the bubble centring phenomenon.

<sup>23</sup>A similar cycle occurs for the gas phase in that gas exits the long bubble’s tail end (pick-up) before entering the subsequent bubble at its nose (shedding).

<sup>24</sup>Indicated also by experiment for air-water slug flow; see figure 8 in [Belt and Leinan \(2015\)](#).

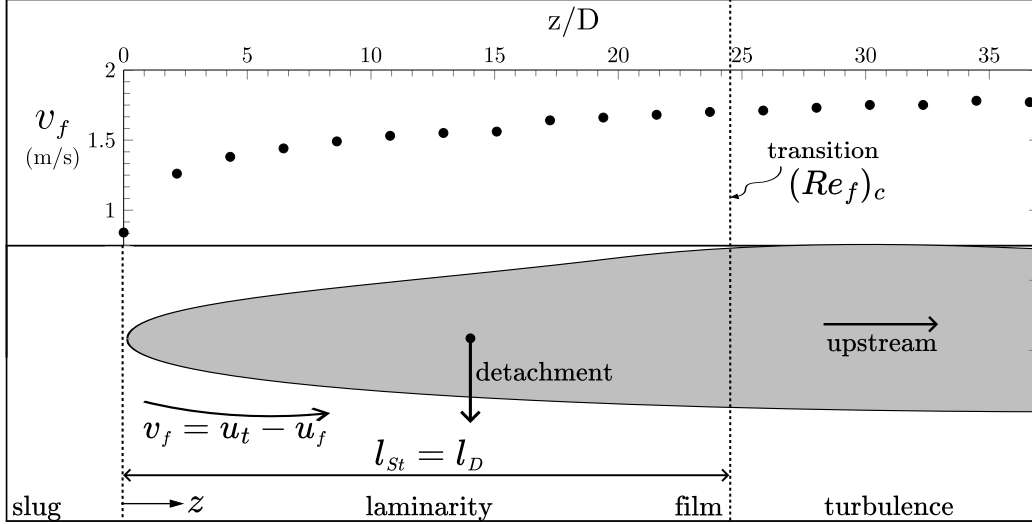


Figure 15: Illustration of a novel hypothesis for partial-centring in horizontal slug flow: film liquid velocity—relative to unit-cell translation—creates two regimes within the film: 1) a downstream laminar region wherein a vertical force can be applied to the corresponding section of bubble, potentially causing detachment and 2) an upstream turbulent region wherein the mode of vertical force transmission is broken. Overlaid are air-water slug flow data from [Belt and Leinan \(2015\)](#) which demonstrate a  $v_f$ -profile in the film; however, centring-configuration and critical film-Reynolds number  $(Re_f)_c$  shown are not empirically based and included for interpretive purposes only.

potential bubble detachment  $l_D$ .<sup>25</sup> In the turbulent film segment  $z \in (l_{st}, l_B]$ , postulated centring events are blocked and detachment cannot occur, thus actualizing the partial-centring configuration. Regardless of its axial extent, film region laminarity does not guarantee the occurrence of long bubble centring—it is simply a necessary condition. As formulated in PL20, centring occurs if the catalyzed downward force is greater than the counteracting

<sup>25</sup>In this theory, there is a possible scenario in which  $l_{st} \neq l_D$ . Envisioning an incremental—rather than summative—vertical force balance applied to the bubble, partial-centring could, hypothetically, occur with  $l_D < l_{st}$  if  $\Sigma F_y(z)$  changes sign before the laminar region desists (with respect to  $z$ ). Thus, the two length metrics are defined separately; however, unless otherwise invoked,  $l_{st} = l_D$  can generally be assumed.

buoyant tendencies acting upon the bubble.<sup>26</sup> Film laminarity thus serves as a modulator in facilitating the centring phenomenon—should the right dynamical conditions exist—as does the existence of a thin upper liquid film.

The outlined theory of partial-centring is seamlessly extrapolated to the case of full-centring; namely, realization of the latter necessitates laminarity throughout the entire axial span of the film region  $z \in [0, l_B]$ —at minimum within the liquid adjacent to the lower gas-liquid interface. For practical and theoretic purposes, an adapted form of Reynolds number—characterizing the laminar-turbulent transition in the film region’s flowing liquid—is desirable. The system of interest features a frame-of-reference affixed to the steadily translating, structurally constant slug unit-cell and, as such, apparent liquid motion traversing the film region from long bubble nose-tip to tail. Therefore, a plausible approach to modelling the dynamic balance between viscous and inertial forces within the film is given by

$$Re_f(z) = \frac{\rho_L v_f(z) h_f(z)}{\mu_L} \quad (23)$$

where  $h_f(z)$  is the film height profile. To determine a numeric value for critical film-Reynolds number  $(Re_f)_c$ , considerable experimental inquiry is needed; regardless, its conceptualization is a valuable tool in differentiating potentialities of partial- and full-centring manifestation. For example, full-centring is realized only if

$$\forall z \in [0, l_B]: Re_f < (Re_f)_c \quad (24)$$

while partial-centring occurs according to

$$\begin{aligned} \forall z \in [0, l_D]: Re_f &< (Re_f)_c \\ \forall z \in (l_D, l_B]: Re_f &> (Re_f)_c. \end{aligned} \quad (25)$$

Using this logic, the demonstrable prevalence of bubble centring in HVL-containing slug flow systems becomes clearly comprehensible. Imagine, as an

---

<sup>26</sup>This explains why superficial rate ratio  $\gamma$  affects realization of bubble centring: input gas supply—and thus long bubble volume and buoyant forces—could be increased while mixture inertia is maintained. Doing so would decrease liquid input and thus velocities relative to bubble motion; however, since the downward force is a function of  $\Delta v_f$ , not  $v_f$ , the exact impact of changing  $\gamma$  on centring is not immediately evident, thus elucidating the inherent complexity present in slug flow.

exemplar, a  $\mu_L$ -elevation of  $\mathcal{O}(10^3)$  relative to the water baseline. Assuming that order-of-magnitude remains constant for  $\rho_L$ ,  $\sigma$  and spatial averages  $\overline{v_f}$  and  $\overline{h_f}$ , average film-Reynolds number  $\overline{Re_f}$  will equivalently experience an  $\mathcal{O}(10^{-3})$  diminishment owing to equation 23. Consequently, the likelihood of equation 24 holding true—necessary for full-centring realization—will increase monumentally; meaning, in conditions otherwise producing an adequately large downward force, film region laminarity enables the centring process to proliferate across the long bubble’s entirety.

#### 4.2. Boundary layer theory

Complications arise in the systemic treatment of relative liquid motion and shear in the film region of horizontal slug flow. Because shear emerges from absolute motion in a wall-bounded flow-system, careful justification must be invoked in utilizing equation 23; namely, gas-liquid and liquid-wall contacts in the film region must be considered. Triviality is encountered in the case of liquid inviscidity wherein friction and thus shear are nullified such that relative and absolute motions can be treated equivalently. This may be a plausible approximation for water-based flows yet is difficultly reasoned for HVLs. PL20 approached this quandary by defining negligible interfacial shear as a phenomenological simplification while stipulating that liquid-wall shear could remain present in the film. Regarding the gas-liquid boundary as an inviscid surface, a Bernoulli energy balance can be applied in a manner inspired by Benjamin (1968), using relative velocities (outputted by TB90) to calculate the pressure profile beneath the bubble. For systems featuring an HVL, informed discernment is necessary in modelling the phasic interface. Liquid-wall and gas-wall shear clearly increase with viscosity regardless of flow-regime (e.g., under Blasius-type friction models—see TB90); interfacial shear, however, is strongly dependent on wave presence as investigated by Tzotzi and Andritsos (2013). From their study on stratified flow, there are three distinct interfacial configurations to consider, the realization of which are contingent on input superficial gas rate  $u_G^s$  compared to critical transition rates  $(u_G^s)_\alpha$  and  $(u_G^s)_\beta$  ( $f_i/f_G$ : ratio of interfacial-to-gas friction factors):<sup>27</sup>

---

<sup>27</sup>The film region in slug flow can be treated as a stratified flow with variable liquid height  $h_f(z)$ . This complicates the numerical approach in that  $f_i/f_G$  must be treated iteratively—changing with  $z$ —particularly near bubble nose. Resolution of  $u_G^s$  in friction factor models is not clear. Plausibly,  $u_G$ —average gas velocity above the interface—makes sense; however, since calculating  $u_G$  requires values of  $f_i/f_G$ ,  $u_G^s$  is likely the best option.

**Smooth interface:** no wave disturbances present; occurs for low input gas rates  $u_G^s < (u_G^s)_\alpha$ ; modelled by

$$\frac{f_i}{f_G} = 1 \quad (26)$$

**2D waves:** small-amplitude, short-wavelength, regular waves; occurs for  $(u_G^s)_\alpha < u_G^s < (u_G^s)_\beta$  only if  $\mu_L^\circ < 20$ ; modelled by

$$\frac{f_i}{f_G} = 1 + 0.35 \left( \frac{h_L}{D} \right)^{0.5} (u_G^s - (u_G^s)_\alpha) \quad (27)$$

**Large amplitude waves:** irregular, large waves (also called roll-waves or Kelvin-Helmholtz waves); occurs for  $u_G^s > (u_G^s)_\beta$ ; modelled by

$$\frac{f_i}{f_G} = 2 \left( \frac{h_L}{D} \right)^{0.1} (\mu_L^\circ)^{0.1} + 4 \left( \frac{h_L}{D} \right)^{0.5} (u_G^s - (u_G^s)_\beta) \quad (28)$$

Summarizing, if the interface is smooth, it can reasonably be modelled using ideal flow theory as  $f_i = f_G$  and  $f_G$  is small since  $\mu_G \ll \mu_L$ ; if waves are present, however, there are two possibilities with respect to interfacial shear for HVL systems: 1) if  $\mu_L^\circ < 20$ ,  $f_i$  is  $\mu_L$ -independent for low  $u_G^s$  yet  $\mu_L$ -dependent for high  $u_G^s$  and 2) if  $\mu_L^\circ \geq 20$ ,  $f_i$  is a function of  $\mu_L$  for all  $u_G^s$ . PL20 bubble centring methodology can be updated for HVL-inclusion by integrating the outlined interfacial shear model into the underlying unit-cell slug model (i.e., TB90), thus altering output of  $v_f$  and  $h_f$  profiles for use in the vertical force balance. In doing so, an inviscid energy balance arguably remains applicable since governing slug flow dynamics are transformed to reflect high- $\mu_L$  conditions. Another approach, potentially useful in tandem, is to introduce an additional head-loss term to account for frictional energy losses, analogous to what is done in [Gokcal et al. \(2009\)](#) wherein analysis from [Benjamin \(1968\)](#) is extended to model long bubble drift velocity for HVL slug flows.<sup>28</sup> Based on data examined here, a smooth interface is typically observed for  $\mu_L^\circ \geq 37.7$  (S24 and K20) while smooth or wavy interfaces are observed for  $\mu_L^\circ \leq 30.4$  (N23); however, a wider range of  $Fr$ -values should be studied to better comprehend trends in boundary configuration.

---

<sup>28</sup>One necessary difference, however, is that the head loss term—denoted  $\Delta$  in [Gokcal et al. \(2009\)](#)—would presumably require opposite signage due to the usage of relative velocity in energy conservation.

Less straightforward to resolve is the role of liquid-wall shear in bubble centring phenomenology—especially for systems featuring an HVL. In verity, a boundary layer (BL) of thickness  $\delta$  will form along the inner pipe wall during slug flow, creating two dynamically unique regimes within the film region: 1) an outer flow immediately underneath the long bubble governed by relative motion and 2) an inner near-wall flow governed by absolute motion and viscous effects.<sup>29</sup> For centring to initiate, then, the two flows must remain distinctly separate; meaning, the film region BL growth rate must be minimal as to not constrict and nullify the outer flow, at least long enough for centring mechanisms to occur. Under this dichotomy, it is reasonable to classify the outer flow as approximately inviscid—particularly if a smooth interface persists.

BL development in horizontal gas-liquid slug flow is complex, nuanced and—to the author’s knowledge—not yet theoretically grounded within the relevant base of literature. Even in temporally evolved flow systems, BL expansion is a function of time. At an arbitrary, spatially-fixed location, the velocity profile above the lower pipe wall—which dictates BL height akin to an overbearing free-stream—changes depending on which slug flow region encapsulates the point. Two alternative spatial metrics are introduced here: 1) the lateral inverse of  $z$ , defined as

$$\chi = l_B - z, \quad (29)$$

which represents film region distance measured downstream of long bubble tail and 2) an axial origin  $\zeta$  fixed near the pipe control volume (PCV) inlet which marks the most upstream position, or starting point, of an arbitrary slug unit’s BL.<sup>30</sup> BL height is thus expressed as

$$\delta = \delta(\zeta, t). \quad (30)$$

The question as to proper placement of  $\zeta$  is explored here. The intuitive approach is to align  $\zeta$  precisely with the PCV inlet. However, a novel hypothesis is formulated here: emergence of a turbulent mixing region—formed due to a hydraulic jump at the connection of slug and long bubble tail—must generate enough turbulent kinetic energy to disrupt and reset BL manifestation. Stated differently, the accelerative pick-up process must convey enough momentum

---

<sup>29</sup>BL: boundary layer.

<sup>30</sup>PCV: pipe control volume—pipe region from phasic inlet to outlet.

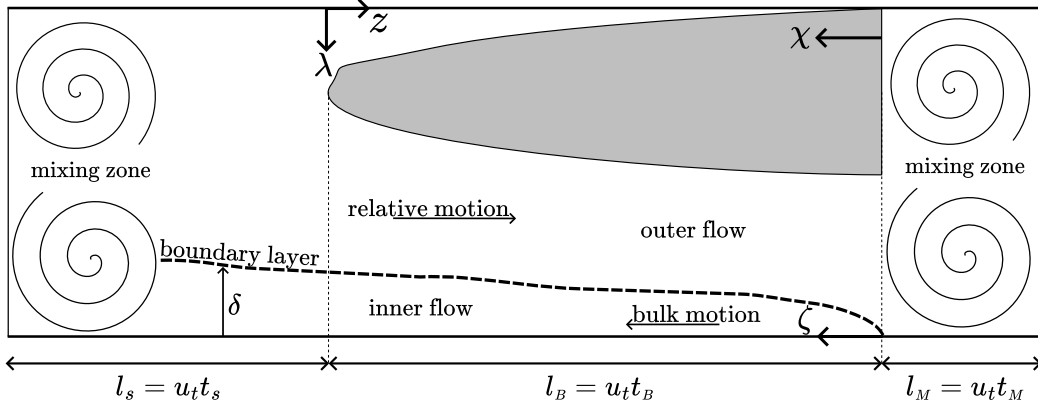


Figure 16: Boundary layer (BL) theory for horizontal gas-liquid slug flow. Depicted are two dynamically unique regions within the film: 1) an outer flow governed by relative motion and 2) an inner flow governed by near-wall viscous effects and bulk/absolute motion. Each unit-cell has an identically formed BL which begins at the first instance of mixing region emergence. Snapshot corresponds to  $\chi = \zeta$ .

to overwhelm and deconstruct coherent structures initiated at PCV inlet and otherwise sustained within the viscous BL. Therefore, the first—as in, most upstream—instance of mixing zone spatiality is defined here as ground-zero for BL development in a slug unit-cell; or,  $\{\delta = 0 \mid \forall t\}$  at  $\zeta = 0$ .<sup>31</sup> Conforming to the notion that every unit-cell is equivalent with respect to geometry and dynamics, mixing regions of conjoining cells are postulated to be segregating limits for BL axial span, as depicted in figure 16 for  $\chi = \zeta$ —conditions at which long bubble tail synchronizes with BL origin. Alternatively viewed, a BL break-up mechanism—such as that put forth above—is resolutely necessary in maintaining ideological sanctity of the unit-cell assumption in that it would disintegrate without.

Established above, separation of inner and outer film flow regions is a fundamental requirement for elongated bubble centring manifestation in that streamlines of relative motion must not be hindered by near-wall, absolute motion-driven viscous effects. Inner flow laminarity is not necessary—BL

<sup>31</sup>This is, of course, a simplification; considering the complexity of slug formation—as, for example, discussed in Taitel and Dukler (1977)—near-wall flow structures may be disturbed at a location upstream of the first fully-developed mixing zone or, alternately, BL destruction may not be complete and artifacts of near-PCV inlet BL may survive the hydraulic jump.

turbulence and bubble detachment could simultaneously prevail so long as dynamic regularity is sustained in the outer flow. Figure 16 illustrates 2-dimensional BL growth in slug flow viewed perpendicular to flow direction; however, pipe geometry requires that 3-dimensional effects must be considered. In the film region, BL growth is cross-sectionally concave in accordance with the lower pipe wall—analogous to an open-channel flow—in effect reducing contact-area between long bubble and outer flow. Assuming that velocity distribution remains unaffected, this impacts centring in that the generated downward force applied to the long bubble decreases in proportion to the resultant decrease in interfacial contact area; thus, detachment conditions  $(Fr)_D$  will be underpredicted without incorporating the inner/outer film flow distinction into modelling methodology.<sup>32</sup>

Figure 17 provides a speculative depiction of cross-sectional BL development at four equally spaced locations within the film, from tail ( $\chi = 0$ ) to nose ( $\chi = l_B$ ) for  $\chi = \zeta + \xi$  where  $\xi$  is a small distance. Evidently, there is an inverse relationship (with respect to  $\chi$ ) between gas-liquid interfacial area and BL extent  $\delta$  in that long bubble nose and tail are exposed to the thickest and thinnest segments of BL, respectively. Thus, as illustrated visually, the tendency of side-wall BL growth to reduce contact-area is minimal at the bubble nose; and, since detachment first occurs at  $\chi = l_B$ , film BL configuration is, seemingly, conducive to centring mechanism transmission. Further, as mentioned earlier, it is crucial to realize that an environment of inner/outer film layer separateness is needed only momentarily, for centring can manifest and then be maintained—by different mechanisms—while BL growth extinguishes the outer flow.

Primarily explored thus far is a temporal snapshot at which long bubble tail aligns with BL origin:  $\chi = \zeta$ . To comprehend the dynamical landscape for all times, the relationship between  $\chi$  and  $\zeta$  must be solidified. Here, an initial time  $t = 0$  is defined in reference to the most upstream genesis of a coherent turbulent mixing region for a singular, arbitrary unit-cell, such that

---

<sup>32</sup>Proof of BL impact on  $(Fr)_D$ : case 1  $\rightarrow$  no BL assumed; case 2  $\rightarrow$  BL inclusion. For a fixed  $Fr$ , assume that  $v_f(z)$ ,  $h_f(z)$ ,  $l_B$  and thus  $\Delta p$  beneath the bubble are equal for both cases. In simple terms,  $F = \Delta p A$  where  $F$  is downward force and  $A$  is contact-area between streamlines and long bubble; thus,  $F_1 = \Delta p A_1$  and  $F_2 = \Delta p A_2$ . Since the film BL decreases contact-area,  $A_2 < A_1$  and  $F_2 < F_1$ ; therefore, if  $Fr = (Fr)_D$  is calculated under the pretence of case 1 (no BL assumed), then an additional  $\Delta Fr$  is needed, in actuality (case 2), to cause detachment. As such,  $(Fr)_D$  is underpredicted.

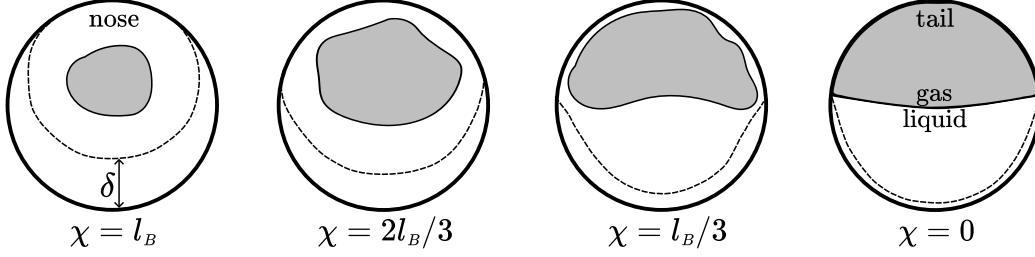


Figure 17: Cross-sectional evolution of hypothetical film region boundary layer at four points throughout the elongated bubble for  $\chi = \zeta + \xi$  where  $\xi$  is a small distance.

a cumulative stretch of a slug region, less its mixing zone, and a film region passes for  $\chi$  and  $\zeta$  to align; or,

$$\chi = \zeta \quad \text{if } t = t_s - t_M + t_B \quad (31)$$

where  $t_B$ ,  $t_s$  and  $t_M$  are times-of-passage for film (long bubble), slug and mixing regions. Dynamical configurations at  $t = 0$  and  $t = t_s - t_M + t_B$  are both depicted in figure 18 wherein, for the former, the unit-cell of interest is not yet in the observational frame. From the above definition of  $\chi = \zeta$ , it stands that

$$\chi = \zeta + u_t (t - t_B - t_s + t_M) \quad (32)$$

or, since  $u_t = l_B/t_B = l_s/t_s = l_M/t_M$ ,

$$\chi = \zeta + u_t t - l_B - l_s + l_M. \quad (33)$$

Within the paradigm constructed here, the film region BL is formed prior to the long bubble's arrival, temporally speaking, for early times  $t \in [0, t_s - t_M + t_B]$  as defined. Depicted in figure 18 at  $t = t_1$ , this phenomenon is conceptualized through careful differentiation between absolute and relative motions in slug flow. Because the turbulent mixing region acts to decay near-wall flow facets—foundationally assumed here—it appears that BL generation occurs in its immediate upstream wake. Since the entire unit-cell structure translates faster than any liquid present, however, the free-stream velocity which first services a fixed BL location  $u_L$  (slug region average liquid velocity) is inevitably replaced by a slower, axially-decreasing free-stream motion  $u_f(z)$  (film region liquid velocity profile). This suggests that, for a point of spatial constancy,  $\delta$  will decrease over time from its originally sustained height—until, that is, it is destroyed entirely by the forthcoming

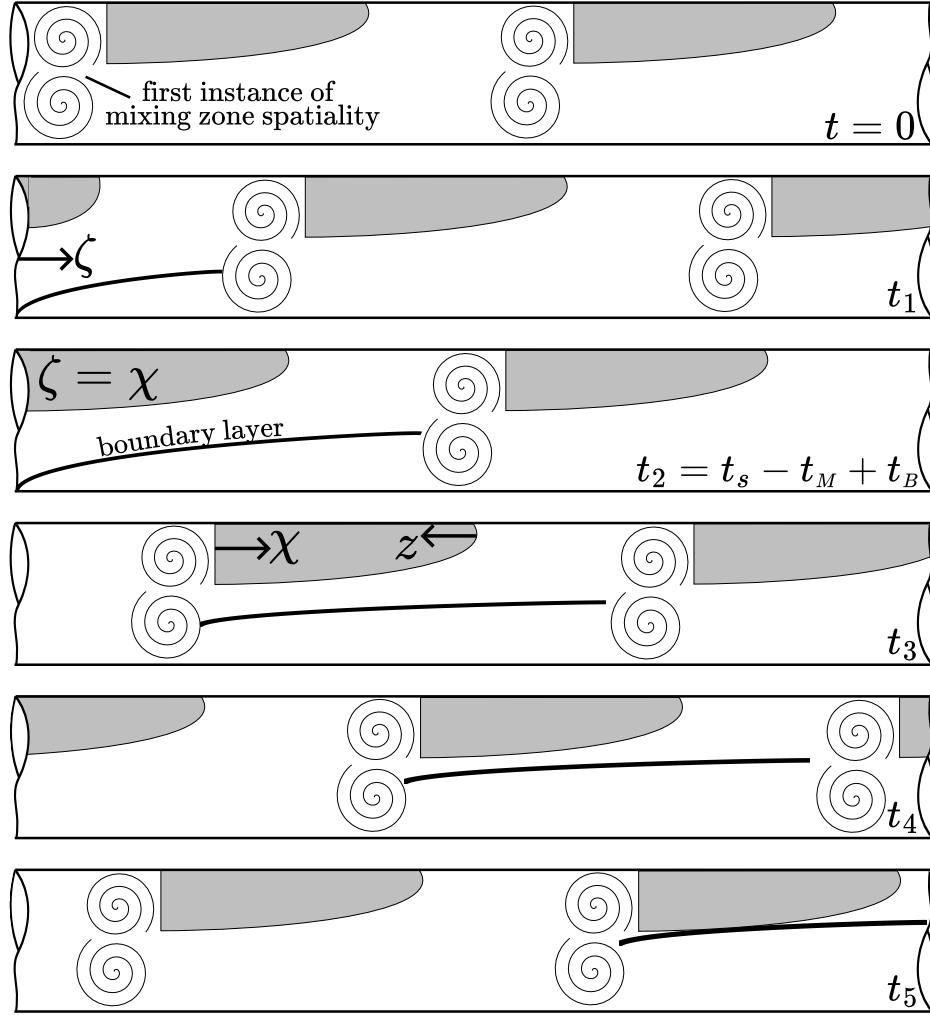


Figure 18: Theoretical depiction of slug flow boundary layer development in time and space for an arbitrary unit-cell.

slug mixing region. Elucidated in figure 18 for  $t > t_s - t_M + t_B$ , the BL is consumed—beginning at its origin—by the approaching turbulent bridge which acts to dissipate inner flow buildup by lifting liquid away from the lower pipe wall. This occurs progressively—as the long bubble translates toward PCV outlet, an equivalent distance of BL is recycled as if being fed through a fluid dynamic shredder; simultaneously, another BL is similarly constructed in the preceding unit-cell, conserving the sanctity of intracellular

sameness. Despite being disrupted at its upstream end, however, BL growth continues until the outer flow is compressed into nonexistence. Such an event represents steady-state developmental status for film BL evolution, analogous to BL convergence beyond a critical distance in a single-phase pipe flow.

In consideration of slug flow BL theory construed here, an alternative form of film-Reynolds number is defined—in replacement of 23—to predict laminarity in the outer flow; namely,

$$Re_f(z) = \frac{\rho_L v_f (h_f - \delta)}{\mu_L}. \quad (34)$$

In parallel, representative logical conditions for non-impingement of the outer flow region—necessary for long bubble detachment—are straightforwardly formulated; for example, full-centring requires that

$$\forall \chi \in [0, l_B]: \delta < h_f \quad (35)$$

while partial-centring corresponds to

$$\begin{aligned} \forall \chi \in (l_B - l_D, l_B]: \delta < h_f \\ \forall \chi \in [0, l_B - l_D]: \delta = h_f. \end{aligned} \quad (36)$$

Obviously, the above conditions alone, if satisfied, do not guarantee perpetuation of centring mechanisms and must be paired with equations 24 and 25—analog counterparts which ascertain outer flow laminarity. Further, 36 does not represent the only probable conditions for partial-centring; for example, 35 could hold true despite the outer flow being axially-divided into laminar and turbulent regions, as in figure 15. Such expressions coincide with a 2D approximation of 3D phenomena in that a cross-sectionally curved BL is quantified using a scalar-valued height  $\delta$ . This is not unreasonable, however, in comparison to historic analytical slug flow models—such as TB90—which utilize unidimensional averaging such that momentum and mass conservation can be simply applied.

To investigate the validity of BL theory put forth here, a case of air-HVL slug flow from Kim and Kim (2023) is utilized. Parameterization is as follows:  $D = 40\text{mm}$ ;  $\mu_L = 37\text{mPa}\cdot\text{s}$ ;  $\rho_L = 878\text{kg}/\text{m}^3$ ; and  $(u_G^s, u_L^s) = (0.6, 1.2)\text{m}/\text{s}$ . The full-form (variable  $h_f$ ) TB90 slug flow model—programmed in MATLAB and validated using air-water data (see figures 11 and 12 of PL20)—was used to calculate film region profiles  $h_f(z)$  and  $u_f(z)$  such that elementary BL

theory could be applied. The published source includes film and slug length data  $l_B$  and  $l_s$ , respectively; thus, calibration was performed using  $l_s$  data and HVL-based closure models as inputs for TB90 and  $l_B$  to gauge output accuracy, in this case obtaining a 6.96% difference between experimental and modelling values. Utilized closure models include:

- $\mathbf{H}_{Ls}$ , slug region holdup: [Kora et al. \(2011\)](#)
- $\mathbf{u}_d$ , long bubble drift velocity: [Jeyachandra et al. \(2012\)](#)<sup>33</sup>
- $\mathbf{C}$ , ratio of max-to-average slug region liquid velocity: [Dukler and Hubbard \(1975\)](#)
- $\mathbf{f}_i/\mathbf{f}_G$ , ratio of interfacial-to-gas friction factors: [Tzotzi and Andritsos \(2013\)](#)
- $\mathbf{u}_t$ , long bubble translational/unit-cell structure velocity: [Nicklin et al. \(1962\)](#)—standard model, given by

$$u_t = C(u_G^S + u_L^S) + u_d \quad (37)$$

Given that BL development in horizontal slug flow is uncharted phenomenological territory, there is an evident lack of appropriate models to predict both  $\delta$  and the distinction between laminar and turbulent near-wall manifestation. Therefore, analysis presented here is a first-order approximation designed primarily to provide proof-of-concept. For example, that a fixed location's free-stream velocity evolves with time suggests that a leading-edge Reynolds number—analogous to that used in flat-plate BL theory—is difficult to define. The simplest approach is to capture instantaneous BL behaviour; namely, to investigate the probable BL profile at  $\chi = \zeta$ . This allows for straightforward allotment of sectional free-stream velocities:  $u_f$  for  $\chi \in [0, l_B]$  and  $u_L$  for  $\chi \in (l_B, l_B + l_s]$ . As such, a leading-edge Reynolds number for slug flow BL growth is defined as

$$Re_\chi = \frac{\rho_L \chi u_\chi}{\mu_L} \quad (38)$$

where

$$u_\chi = \begin{cases} u_f(\chi), & \chi \in [0, l_B] \\ u_L, & \chi \in (l_B, l_B + l_s]. \end{cases} \quad (39)$$

---

<sup>33</sup>Parameterization ranges used to derive correlations for  $H_{Ls}$  and  $u_d$  used here ( $D = 50.8\text{mm}/\mu_L^\circ \in [181, 587]$  and  $D \in [50.8, 152.4]\text{mm}/\mu_L^\circ \in [154, 594]$ , respectively) do not include values used by [Kim and Kim \(2023\)](#); however, extrapolation is assumed to yield reasonable accuracy, confirmed through successful prediction of  $l_f$  (TB90 is highly-sensitive to closure model inputs).

In regard to a critical value of  $Re_\chi$  which differentiates laminar and turbulent BL realization and a calculatory procedure for  $\delta$ , there exists no precedent for horizontal slug flow; therefore, flat-plate BL theory is used here to roughly probe the given conceptual framework’s potential validity. For a constant free-stream velocity flowing over a leading-edge, horizontally-oriented flat-plate, a range for transitional  $Re_\chi$  is given by  $3 \times 10^5 \leq (Re_\chi)_c \leq 3 \times 10^6$ , depending on outer-flow perturbation, while the most commonly used criterion is

$$\begin{aligned} (Re_\chi)_c < 5 \times 10^5: & \quad \text{laminar BL} \\ (Re_\chi)_c > 5 \times 10^5: & \quad \text{turbulent BL} \end{aligned} \tag{40}$$

as per [Schlichting and Gersten \(2000\)](#) (SG00).<sup>34</sup> Applying 38 and 39 to the aforementioned HVL slug flow case, maximum and average values of  $Re_\chi$  in the film region are found to be 13,136 and 5596, respectively. Regardless of the precise numerical value of  $(Re_\chi)_c$ , these numbers are indicative of a laminar BL; although, given that a long bubble travels a significant distance between PCV inlet and outlet, it is plausible that BL growth will adopt turbulence later in the pipe. This should not affect the centring phenomenon, however, since the detachment process likely occurs in early (upstream) sections of the PCV, some length beyond slug formation.

Due to an otherwise lack of necessary literature, laminar flat-plate BL theory from SG00 is used—in tandem with the calibrated TB90 unit-cell slug model—to approximate BL thickness for  $\chi = \zeta$  and, by extension, to determine whether an outer film flow can be maintained for centring to initiate.<sup>35</sup> A concise overview of relevant BL theory from SG00 is given here using appropriate film region parameterization. Inertial force per unit volume of liquid is given generally by

$$F_I = \rho_L \frac{Du_f}{Dt} \tag{41}$$

---

<sup>34</sup>SG00: [Schlichting and Gersten \(2000\)](#) text on boundary layer theory fundamentals.

<sup>35</sup>An attempt was made to upscale laminar flat-plate BL theory from SG00 to an open-channel pipe flow; however, despite being set-up with appropriate geometry, the results were too complicated to feasibly be incorporated into this study. As such, a novel BL model for slug flow is left for future publication.

where  $D/Dt = \partial/\partial t + \mathbf{u} \cdot \nabla$  is the material or total derivative. TB90 is steady-state and 1-dimensional; thus, 41 becomes

$$F_I = \rho_L u_f \frac{\partial u_f}{\partial \chi}. \quad (42)$$

Frictional force per unit volume is given by

$$F_F = \frac{\partial \tau_f}{\partial y} \quad (43)$$

where  $\tau_f$  is film shear stress and

$$y = D - \lambda \quad (44)$$

is the spatial inverse of  $\lambda$ , as already defined. Assuming a Newtonian liquid, 43 is rewritten using the standard law of viscosity as

$$F_F = \frac{\partial}{\partial y} \left( \mu_L \frac{\partial u_f}{\partial y} \right) = \mu_L \frac{\partial^2 u_f}{\partial y^2}. \quad (45)$$

Scaling  $y \sim \delta$ , inertial and frictional forces are equated  $F_I = F_F$  using 42 and 45 to yield

$$\delta \sim \sqrt{\frac{\mu_L \chi}{\rho_L u_f}}. \quad (46)$$

Defining  $\delta = \delta_{99}$  where  $\delta_{99}$  is BL height at which local velocity reaches 99% of free-stream velocity, proportionality for 46 is determined to be

$$\delta(\chi) = 5 \sqrt{\frac{\mu_L \chi}{\rho_L u_f}} \quad (47)$$

based on the original Blasius (1908) solution.<sup>36</sup> Also of interest is displacement thickness  $\delta_1$ —conceptualized as the vertical shift imparted on the outer flow by the BL relative to the inviscid baseline, given here by

$$\delta_1(\chi) = 0.34\delta(\chi). \quad (48)$$

Results of the slug flow BL micro-study—including  $h_f$ ,  $Re_f$  and film region  $\delta$  and  $\delta_1$  for the selected flow-case from Kim and Kim (2023)—are shown in

---

<sup>36</sup>As reported by SG00 (p.31).

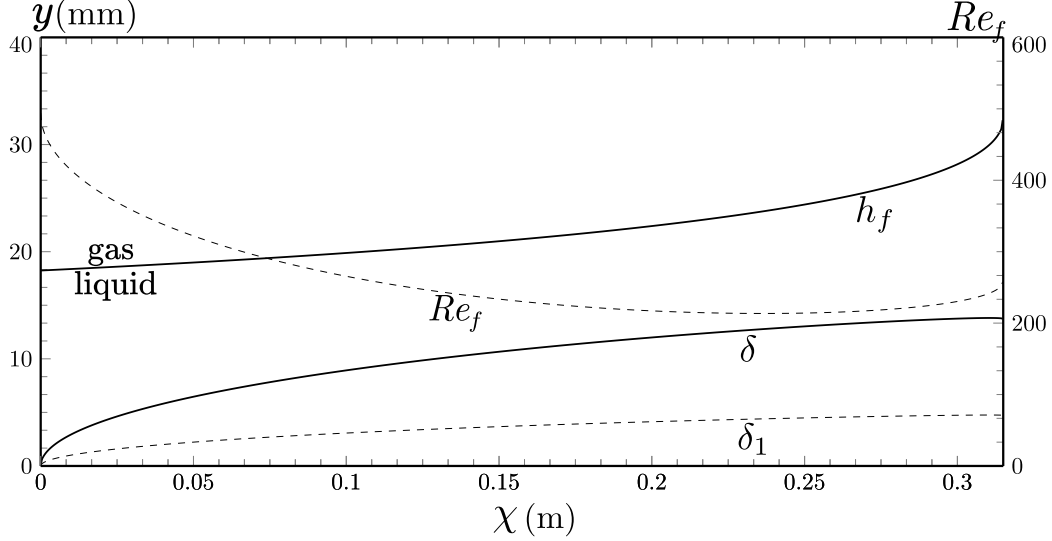


Figure 19: Slug flow boundary layer theory applied to HVL case from [Kim and Kim \(2023\)](#):  $D = 40\text{mm}$ ;  $\mu_L = 37\text{mPa}\cdot\text{s}$ ;  $\rho_L = 878\text{kg/m}^3$ ;  $(u_G^s, u_L^s) = (0.6, 1.2)\text{m/s}$ . Full-form [Taitel and Barnea \(1990\)](#) (TB90) model used with  $l_s$  data and appropriate closure models to calculate  $h_f$  and  $u_f$  profiles;  $l_B$  data used to validate calibration. Equations 47, 48 and 34 used to output  $\delta$ ,  $\delta_1$  and  $Re_f$ , respectively. Flow scenario corresponds to  $\chi = \zeta$ .

figure 19 wherein the  $y$ -axis span represents inner pipe diameter. Observed from the  $Re_f$  profile (obtained using equation 34) is an unusual trend; namely,  $Re_f$  reaches a minimum (213.5) at  $\chi = 0.75l_B$  rather than at bubble nose-tip—as would be predicted by 23. Furthermore, a maximum value of 494 is found at long bubble tail, indicating that the entire outer film flow exists in laminarity. Combined with a notable modelled separation between gas-liquid interface and the BL, this suggests a dynamic environment facilitative for bubble centring realization. Whether this case indeed demonstrates significant detachment is unknown since photographic data are not available; regardless, the above application clearly elucidates the importance of incorporating BL theory into any analytic framework for bubble centring.

#### 4.3. Wedge theory

Thus far, film region laminarity has been a postulated prerequisite for the initiation of long bubble centring in horizontal slug flow; however, turbulence is likely in air-water and low-HVL flows. An alternative mechanism—termed liquid wedging—is put forth here as a causal element in the realization of

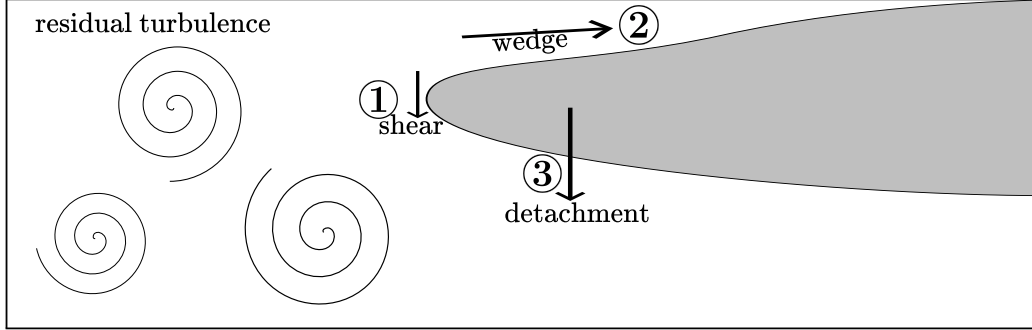


Figure 20: Depiction of the wedge theory for partial-centring, comprised of three chronological sub-mechanisms: ① residual turbulence in the preceding slug region enacts downward shear on long bubble nose-tip, resulting in slight detachment from upper pipe wall; ② relative slug motion causes liquid to enter space created between long bubble and upper pipe wall, driving a wedge-like expansion; and ③ substantial bubble detachment occurs, manifesting the partial-centring flow configuration.

partial-centring under certain dynamic conditions. A novel theory, visually represented in figure 20, is presented as a conglomeration of three distinct flow events. Summarized, they are:

1. **Nose shear:** turbulence in the downstream slug region—stemming residually from mixing region eddies—contacts long bubble nose due to relative motion, detaching it slightly from the upper pipe wall due to transmission of downward shear;
2. **Liquid wedging:** liquid enters the created gap with wedge-like shape; and
3. **Detachment:** since the gas structure is deformable, a segment of the bubble is driven toward pipe centreline, thus manifesting the partial-centring configuration.

The described process is compounding yet limited—as part of the bubble is centred, the overlying liquid wedge cumulatively accrues volume, thus perpetuating the cycle. However, at some level of detachment, the dual-channel fluid connectivity between wedge and underlying film reaches critical fluency in that proliferation of centring mechanisms cease and a localized steady-state emerges. Since the hypothesized chain of wedging mechanisms is functionally dependent on turbulence immediately downstream of long bubble nose, both inertial input  $Fr$  and liquid viscosity  $\mu_L$  are modulators. For similar  $Fr$ -characterization, flows with higher  $\mu_L$  incur lower turbulence intensity in

the slug mixing region. Further, turbulent kinetic energy dissipation rate  $\epsilon$  is positively proportional to  $\mu_L$  (Pope, 2000),

$$\epsilon \sim \mu_L; \quad (49)$$

therefore, turbulence in the slug mixing zone diffuses faster for high- $\mu_L$  systems. As such, the likelihood of eddies reaching the long bubble nose with enough energy to catalyze the wedging process is reduced in HVL systems. For this reason, the presented theory is plausibly more applicable to water-based or low-HVL slug flows wherein film region laminarity may not be satisfied. In certain  $\mu_L$ -cases, wedging may occur concurrently with the PL20 streamline mechanism; however, cut-off valuation is subject to experimental and further theoretical inquiry. For medium- or high-HVL flow-cases wherein film laminarity is expected, the aforementioned streamline centring model is likely most appropriate for usage. Another aspect of wedge theory to consider is that of eddy rotational orientation near long bubble nose—within context supplied here, turbulent eddies must rotate such that downward shear is applied to bubble nose-tip, suggesting a potential element of randomness.

#### 4.4. The slug-annular transition

Evidently, the bubble centring phenomenon plays a significant role in the microcosm of horizontal gas-HVL slug flow dynamics. Here, it is subsequently hypothesized to host vital functionality within the broader sphere of flow pattern transition theory for HVL-featuring systems. In §1 it was shown that, for at least two sets of HVL data with  $\mu_L^\circ \in [1, 11000]$ , predictive ability of the classical TD76 mechanistic model deteriorates exponentially with increasing  $\mu_L$ . For one of the utilized sources, Matsubara and Naito (2011), it was further determined that the portion of wrongly predicted flow patterns which involve either slug or annular regimes increases with  $\mu_L$ .<sup>37</sup> A different study from Gokcal et al. (2008) (G08)—which reports HVL flow pattern data for  $\mu_L^\circ \in \{181, 587\}$  and  $D = 50.8\text{mm}$  overlaid with mechanistic modelling predictions—is invoked to expand upon the picture illustrated in figure 1.<sup>38</sup>

---

<sup>37</sup>This conclusion was found in exclusion of the baseline air-water case. Also, with respect to the data source, the range of investigated  $(u_G^s, u_L^s)$  narrows upon each incremental increase in  $\mu_L$ ; thus, it is unclear if the trend in question genuinely represents a focused weakening of predictability or, instead, is an artifact of non-constant experimental design.

<sup>38</sup>G08: Gokcal et al. (2008) HVL flow pattern study.

G08 utilizes flow pattern transition models from Barnea (1987) (B87) and Zhang et al. (2003) (Z03), both of which are unified or inclination-flexible. When collapsed onto horizontal pipe systems, B87 is a derivative of TD76; Z03, however, is founded on slug flow dynamics and thus is dependent on correlative closure models.<sup>39</sup> Also included in G08 is a modified form of the Z03 model (Z03M) which implements an artificial modulator to correct the “momentum term for gas entrapment.”<sup>40</sup> Experimental HVL flow pattern data and modelling predictions from B87, Z03 and Z03M—recreated from G08—are given in figures 21 and 22. Overlaid lines and sectional labels represent modelling predictions; discrete points are experimental data. Note that Z03 combines stratified and annular (ST/AN) flows while B87 differentiates between them. The latter also segregates slug ( $H_{Ls} \neq 1$ ) and elongated bubble ( $H_{Ls} = 1$ ) flows.

In general, modelling predictability is observed to worsen across the  $\mu_L$ -increase of  $\Delta\mu_L^\circ = 406$  (+105.7%) for G08 flow pattern data, reiterating the trend explored through figure 1. Also supported is the notion that the slug-annular boundary is poorly predicted, in particular, for HVL-systems. This is visualized in figure 23 which displays, in bar-chart format, the percentage of total experimental slug or annular flow-points—for both  $(\mu_{L1}, \mu_{L2}) = (181, 587)$ —that were wrongly predicted by each of the tested mechanistic models. For example, B87-SL is percentage of slug points wrongly predicted by B87. Z03M, in essence, implements a manual workaround to improve data predictions, suggesting that bettered capacity does not reflect a more robust alignment with underlying mechanics; thus, B87 and Z03 are primarily of interest. Regardless, the takeaway remains unchanged with its inclusion—systemic amplification of  $\mu_L$  in a horizontal gas-liquid pipe flow wreaks havoc on the generalized ability to predict flow pattern occurrence, particularly at the slug-annular boundary.

Based on G08 modelling endeavours, it appears that increasing  $\mu_L$  alters the range of superficial flow rates for which slug flow is predicted; however, such changes are not reflected in the data, resulting in worsening flow pattern calculation. Specifically, in this case,  $\Delta\mu_L$  expands—on a flow pattern map—the outputted slug region at both stratified/non-stratified and slug/annular boundaries while simultaneously constricting it at the

---

<sup>39</sup>B87 and Z03: Barnea (1987) and Zhang et al. (2003) flow pattern transition models.

<sup>40</sup>Z03M: G08-modified form of Z03 model.

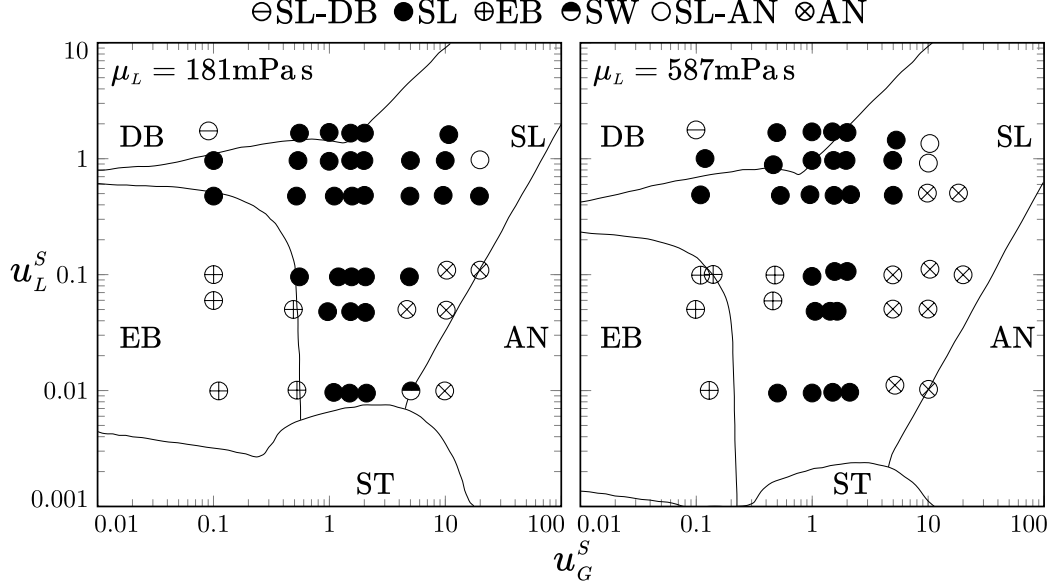


Figure 21: HVL flow pattern data from Gokcal et al. (2008) (G08) overlaid with predictions from the Barnea (1987) (B87) mechanistic transition model. Above legend corresponds to experimental points; directly labelled regions correspond to model predictions. SL=slug; EB=elongated bubble; DB=dispersed bubble; ST=stratified (smooth or wavy); SW=stratified-wavy. Hyphenated legend entries are transitional. Units for superficial velocity are m/s. Adapted from figures 7 and 9 of original source.

slug/dispersed bubble transition, producing a net accumulation. The data, however, show a lesser change. For reference, across  $\Delta\mu_L$ , G08 data show a decrease in measured slug (or elongated bubble) flow points from 36 to 33 (82% to 73% of total points) and an increase in annular points from 5 to 9 (11% to 20% of total points). Another relevant inference drawn from G08 stems from their empirical definition of a slug-annular transitional flow pattern (labelled SL-AN; registered once and twice for  $\mu_L^\circ = 181$  and  $\mu_L^\circ = 587$ , respectively). A qualitative description is not given; intuitively, the superposition of slug and annular regimes will, however, exhibit both intermittency and—at least somewhere within the PCV—a competent liquid film enclosing a gas core with non-negligible thickness. Such a depiction clearly coincides with slug flow featuring fully-centred long bubbles in that both periodicity and annularity

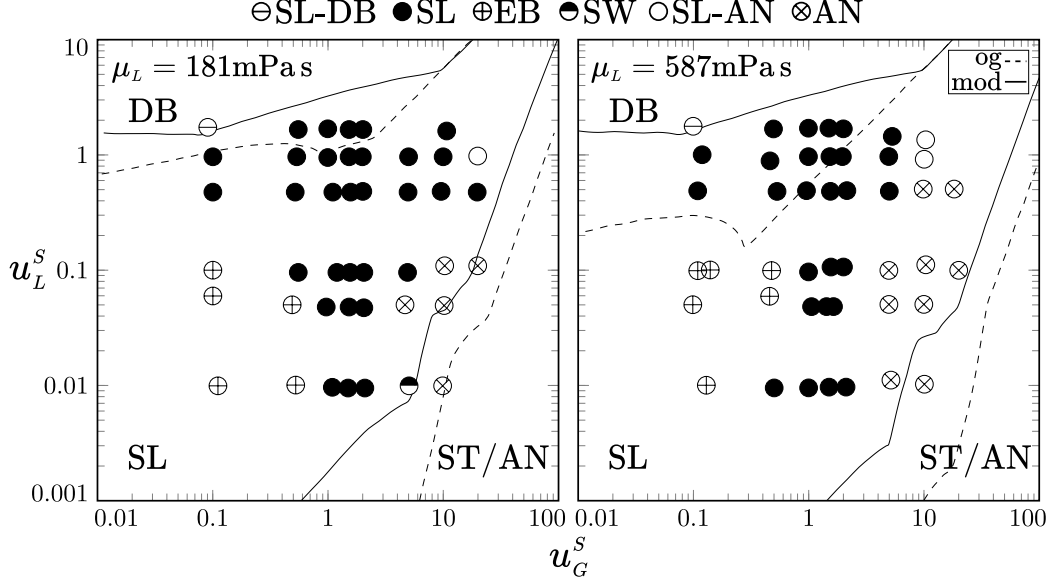


Figure 22: HVL flow pattern data from Gokcal et al. (2008) (G08) overlaid with predictions from the Zhang et al. (2003) (Z03) mechanistic transition model and its modified form (Z03M) from G08. Dashed lines represent Z03; solid lines represent Z03M. Above legend corresponds to experimental points; directly labelled regions correspond to model predictions. SL=slug, EB=elongated bubble, DB=dispersed bubble, ST=stratified (smooth or wavy), SW=stratified-wavy. Hyphenated legend entries are transitional. Units for superficial velocity are m/s. Adapted from figures 11 and 12 of original source.

are observed.<sup>41</sup> All noted SL-AN designations are encountered at the largest ( $u_G^s, u_L^s$ ) pairs of their respective flow pattern maps—logically corresponding to the most significant degree of incurred centring. The above observations may indicate a critical role of bubble centring in the slug-annular transition for HVL systems—one that seemingly lacks field-scale recognition.

<sup>41</sup>That SL-AN points are observed sparsely, relative to other flow patterns, could imply that centring is not present in the majority of slug flow data; however, centring occurs on a wide spectrum and perfect-centring (radial symmetry—as is likely found in SL-AN data) is not a prerequisite for centring classification. Further, detection can be tricky—if flow pattern identification is completed visually, compared to using, for example, advanced image processing techniques, lesser degrees of centring may not be recognized. For relatively small separation distances (i.e.,  $\lambda_K < 0.1D$  yet non-zero) most researchers would plausibly observe slug rather than transitional flow, especially considering that the phenomenological study of centring is still developing.

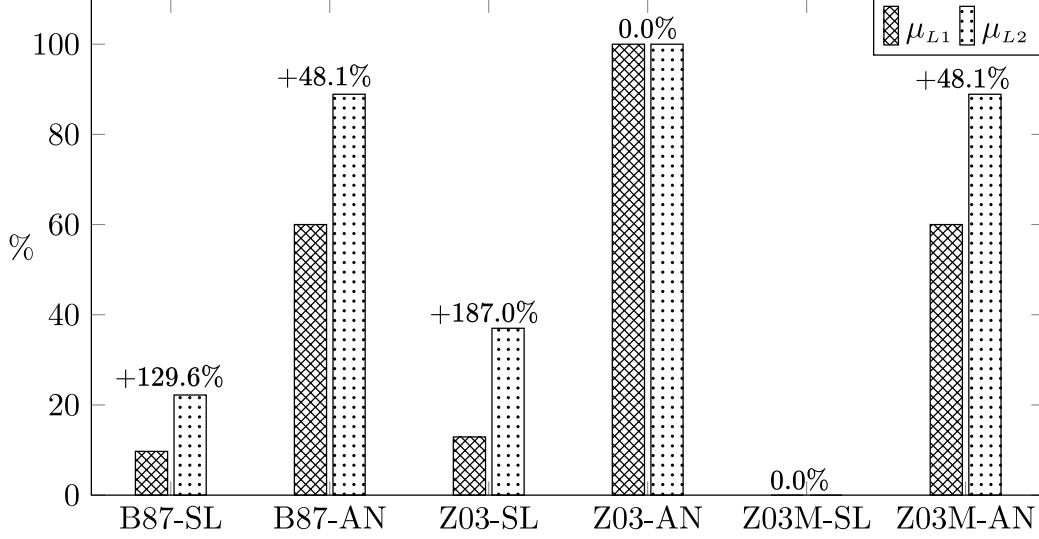


Figure 23: Percentage of total experimental slug (SL) and annular (AN) flow-points from Gokcal et al. (2008) (G08) that were wrongly predicted by Barnea (1987) (B87), Zhang et al. (2003) (Z03) and modified-Z03 (Z03M) mechanistic models where  $\mu_{L1} = 181\text{mPa s}$  and  $\mu_{L2} = 587\text{mPa s}$ . Overlaid are %-difference values which represent changes due to  $\Delta\mu_L$ .

Priorly given analyses firmly demonstrate the need for fresh perspective in the realm of HVL flow pattern transition theory. Combined with the observed transitory flow pattern described above, two elements of reasoning suggest that a novel paradigm for the slug-annular boundary can be construed through incorporation of the bubble centring phenomenon: 1) deterioration of existing mechanistic models' predictive capacity when applied to the slug-annular boundary, positively proportional to  $\mu_L$  and 2) an empirically verifiable connection between full-centring and increasing- $\mu_L$ . A unique theoretical framework—designed particularly for HVL-containing systems—is derived here qualitatively. Two key mechanisms, both related to elongated bubble dynamics, are invoked:

**Detachment:** initiation of long bubble centring

**Coalescence:** establishment of bulk gas continuity

Figure 24 illustrates the theory using four snapshots of an identical pipe and fluid configuration wherein liquid input  $u_L^S$  is fixed and gas supply  $u_G^S$  increases incrementally starting from ①. All four  $u_G^S$ -cases exist under temporal development with stratified flow near the PCV inlet (not shown).

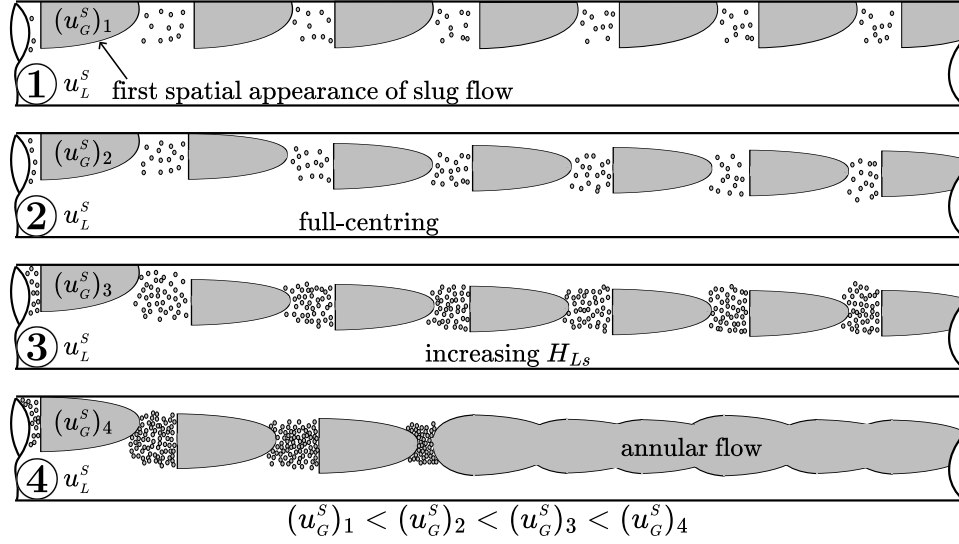


Figure 24: Illustration of novel mechanistic framework for the slug-annular transition, designed for gas-HVL flow systems using four snapshots at incrementally larger superficial gas rates and a fixed liquid rate: ① traditional slug flow; ② full-centring beyond interfacial instability; ③ increases in slug holdup and degree of centring; and ④ coalescence occurring after centring, resulting in annular flow pattern.

At some arbitrary distance beyond the inlet, an interfacial instability occurs which, in all instances, triggers the manifestation of non-centred slug flow for differing lengths of pipe. As such, the left-most elongated bubble in ① to ④ represents the first spatial appearance of slug flow. Evolution is as follows:

**Case ①** Typical manifestation of intermittency—termed here traditional slug flow—with minimal long bubble centring.

**Case ②** Traditional slug flow exists beyond the interfacial instability; however, an increase in relative motion caused by  $\Delta_{12} = (u_G^s)_2 - (u_G^s)_1$ , combined with laminarity in the film, results in long bubble detachment and full-centring prevails for the remainder of the PCV. A slight increase in slug holdup  $H_{Ls}$  is incurred.

**Case ③** Traditional slug flow exists momentarily before long bubbles detach and nearly-perfect, radially symmetric centring is sustained. The further increase in gas inertia  $\Delta_{23} = (u_G^s)_3 - (u_G^s)_2$  causes another notable increase in  $H_{Ls}$  such that it approaches yet falls below a critical limit for coalescence  $(H_{Ls})_c$ .

**Case ④** Traditional slug flow emerges for an instant, likely with some degree of partial-centring. Beyond that, owing to maximal relative gas motion induced by  $\Delta_{34} = (u_G^s)_4 - (u_G^s)_3$ , long bubbles are immediately centred; however, significant gas volume is dispersed in the liquid slugs with  $H_{Ls} > (H_{Ls})_c$  and thus gas coalesces into a continuous bulk structure. Because centring occurs upstream of coalescence, the gas core flows with a film surrounding its radial entirety; as such, annular flow is maintained for the PCV’s majority. Due to the means of coalescence—periodic consolidation of curved (nose) and flat (tail) topologies—the gas-liquid interface is probably wavy as depicted in figure 24.

One potentially contradictory aspect of this theory is the existence of both slug and annular flow patterns in the same flowing pipe, as in ④, which defies an axiom put forth in TD76; namely, equilibrium stratified liquid height  $h_L$ —compared to a critical value—alone differentiates the two emerging configurations. If  $h_L > (h_L)_c$ , enough liquid is said to exist at a Kelvin-Helmholtz instability for a stable liquid bridge or slug to form; if  $h_L < (h_L)_c$ , the liquid is said to be swept around the inner pipe wall to form an annular film.<sup>42</sup> The contradiction can be reconciled, however, in realizing that—in the novel theory—slug flow exists only briefly before devolving into annularity. Further, because liquid supply remains constant in all four flow-cases, one could argue that if a competent reservoir exists in case ①, it can hypothetically exist in case ④. Also, to the author’s best knowledge, there exist no visual data within the literature base that depict and thus confirm the phenomenological distinction put forth in TD76. The principle utilized here is divergent by design since, for novel paradigms to become solidified, accepted fundamentals must be challenged.

Regarding calculatory procedure, the presented slug-annular framework can be formulated as a combination of bubble centring and coalescence models specifically calibrated and validated for HVL systems. For the former, PL20 is a logical starting point, albeit requiring upscaling for HVL inclusion as described in §4.2. For the latter, the B87 model—utilized in G08—offers useful

---

<sup>42</sup>For reference, TD76 suggests  $(h_L)_c = 0.5D$ ; however, a subsequent study from Barnea et al. (1982a) concludes that  $(h_L)_c = 0.35D$  is appropriate, at least for air-water flow systems. For HVL systems, a recent study by Al-Safran and Al-Qenae (2018) reports, based on empiricism, that  $(h_L)_c = 0.45D$  is functional. That modern research is still utilizing this simplistic approach is telling in that a sophisticated model is lacking.

parallels; namely, in assuming annular flow to exist, a critical gas core holdup is invoked to determine whether a conversion to stable intermittency will occur (Barnea, 1986; Barnea et al., 1982b; Barnea and Brauner, 1985).<sup>43</sup> Based on rudimentary packing theory, B87 posits that  $(H_{Ls})_c = 0.24$  represents the slug-annular boundary; however, this criterion is unsubstantiated for HVL systems (as demonstrated priorly). Considering the dynamically unique flow scenarios depicted here, it is plausible that other mechanisms may hold an active role; thus, further research into long bubble coalescence is necessary.

## 5. Finalities

Based on empirical and theoretical analyses provided throughout this paper, the following conclusions and suggestions for further work are drawn with respect to horizontal gas-liquid pipe flows:

### 5.1. Conclusions

1. Elongated bubble centring is strongly correlated with liquid viscosity  $\mu_L$ ; specifically, the degree of incurred centring is positively proportional to  $\mu_L$  as evidenced by thorough analyses of datasets extracted from Naidek et al. (2023) (N23;  $\mu_L \in [1, 30.4]$ mPa s), Shin et al. (2024) (S24;  $\mu_L \in [37.7, 352]$ mPa s) and Kim et al. (2020) (K20;  $\mu_L \in [510, 960]$ mPa s).
2. Full-centring—defined as non-negligible separation between upper pipe wall and elongated bubble realized throughout the entire film region in slug flow—is a highly-probabilistic occurrence for systems with  $\mu_L \geq 352$ mPa s in that it prevails even in low-inertial conditions  $Fr \geq 0.57$ . This is contradictory to air-water dynamics under which full-centring is observed in high- $Fr$  flows only.
3. Despite predominance in past literature, long bubble nose-tip position  $\lambda_N$  is deemed a non-ideal measure of centring extent due to an inherent level of high-variability; instead, separation distances 1- and 2-diameters upstream of nose-tip  $\lambda_{1D}$  and  $\lambda_{2D}$  along with body and tail separation  $\lambda_B$  and  $\lambda_T$  are recommended for determination of incurred degree of long bubble centring.

---

<sup>43</sup>B87 includes an additional mechanism for the slug-annular boundary; that is, a dynamic instability within the film causes flow reversal and blockage due to buildup. However, in collapsing the unified model onto the case of a horizontal pipe, the critical holdup mechanism is deemed solely relevant.

4. The largest extent of bubble centring measured in this study is found in a flow-case with both high- $Fr$  and high- $\mu_L$ ; namely, case B.2 from the S24 dataset with  $(Fr, \mu_L) = (2.94, 352\text{mPa}\cdot\text{s})$  exhibits nearly perfect-centring (radial symmetry), particularly in the nose region.
5. Elaborating on the phenomenological framework put forth in [Perkins and Li \(2020\)](#) (PL20), causality in the measurable interconnection between bubble centring and  $\mu_L$  is investigated; namely, a foundational assumption utilized in the PL20 model—that coherent streamlines of relative motion immediately underneath the long bubble allow for generation of a downward force necessary in the initiation of centring—is intrinsically applicable to HVL systems because laminarity persists, in general, for low- $Re$  and thus high- $\mu_L$  flows.
6. Considering that shear in a wall-bounded flow stems from absolute motion, liquid in the film region of slug flow is conceptualized as a dual-layer configuration: 1) a near-wall boundary layer (BL) governed by absolute velocity  $u_f$  and 2) a near-bubble outer flow governed by relative velocity  $v_f = u_t - u_f$ . For the PL20 streamline mechanism to unfold, the outer flow must be unimpeded by the BL, at least momentarily; and, film laminarity can be determined using a Reynolds number with characteristic length  $h_f - \delta$ .
7. A novel theory for BL development in horizontal slug flow—consistent with unit-cell methodology—is postulated by assuming that the slug’s turbulent mixing region acts to deconstruct and recycle near-wall structures, thus serving to segregate individual unit-cell BL growth. As the long bubble translates downstream, the BL is hypothesized to continually grow while simultaneously being destroyed at the upstream mixing zone—eventually restricting the outer flow entirely at a localized steady-state limit.
8. The posited BL theory is tested using a calibrated case of HVL slug flow. Film height and velocity profiles are calculated using the [Taitel and Barnea \(1990\)](#) (TB90) unit-cell model with appropriate closure inputs while BL thickness is approximated using flat-plate theory. Results demonstrate a significant differentiation between inner and outer film flow regions which—along with predicted film laminarity—suggests conditions favourable for manifest bubble detachment.
9. Two potential mechanisms are explored in connection to partial-centring realization: 1) an axial transition from laminarity into turbulence within the film outer flow at a critical  $v_f$  or  $Re_f$  which negates relative motion

streamlines and 2) residual slug region turbulence causing downward shear on long bubble nose-tip which drives it toward the pipe centreline while liquid flows like a wedge into the created gap—an effect that is compounding yet limited. Film laminarity modulation is predominantly applicable to HVL flows; liquid wedging can be active even for a turbulent film, making it relevant for water-based or low-HVL flows.

10. Demonstrated using HVL flow pattern data from Matsubara and Naito (2011), Zhao et al. (2013) and Gokcal et al. (2008) is a deterioration of mechanistic models' predictive capacity, positively proportional, in general, to  $\mu_L$  as evidenced using outputs from Taitel and Dukler (1976) (TD76), Barnea (1987) (B87) and Zhang et al. (2003) (Z03). In particular, the slug-annular boundary is inaccurately calculated for HVL systems—an effect that amplifies with increasing  $\mu_L$ .
11. The mechanistic approach is, intrinsically, to capture underlying phenomena; thus, a knowledge gap in the realm of gas-HVL flow dynamics is elucidated through non-successful application of commonly utilized models. As such, a novel theoretical framework for the slug-annular transition in HVL systems is derived, qualitatively, as a function of two unique long bubble mechanisms: centring and coalescence. In this paradigm, annular flow emerges from slug flow when full-centring occurs prior to coalescence in a temporally-developed flowing pipe system.

## 5.2. Future work

1. The field of multiphase pipe flow research will benefit significantly from a purposeful influx of purely theoretical works. To believe that powerhouse investigators of decades past (e.g., Barnea, Taitel, Dukler, Brauner and others) left behind a state of complete phenomenological determination is, although understandable, fallacious as indicated by a demonstrable lack of accuracy in modelling horizontal gas-HVL flow pattern data. Presently, the subfield is characterized by an abundance of experimental studies utilizing a wide variety of operational conditions, fluid profiles and pipes; necessary, going forward, is reestablishment of balance through careful innovations in novel mechanistic inquiry, capitalizing on the large girth of available exotic data, analogous to 1970-90—a remarkable era in the development of air-water theory.
2. A rigorous empirical study focused on the bubble centring phenomenon would bring tremendous value to the field. Variables of interest include Froude number, superficial rate ratio, liquid viscosity, operating

pressure, rheological profile, pipe size and inlet configuration. Novel illumination and signal processing techniques are needed to visually capture and measure centring metrics at bubble nose, body and tail and 3-dimensional images can be obtained using methods such as those described in [Jamari et al. \(2008\)](#). Different regions of the flowing pipe system—such as near-inlet and far-downstream—and temporal effects should be considered to better understand centring development. Ultra high- $\mu_L$  fluids ought to be included to enhance servicing of the heavy oil industry; for example,  $\mu_L \in [1000, 50000]\text{mPa}\cdot\text{s}$ .

3. Using appropriate alterations suggested in §4.2, the baseline PL20 centring model must be scaled and tested for HVL system viability. Partial-centring theory put forth here and in PL20 must be validated and expanded upon, considering the phenomenological roles of thin upper film extent, film laminarity and BL growth. Robust distinction between a thin upper film and bubble centring should be clarified, particularly for HVL slug flow wherein detachment may be observed in low- $Fr$  conditions. Generally speaking, centring theory must be continually developed such that the phenomenon exits obscurity into the light of comprehension.
4. Further work is required to understand BL generation in horizontal slug flow, particularly as it relates to bubble centring mechanics. Dedicated experimental and simulation studies would compound theoretical discussion posed here. Particle image velocimetry or dye injection can be used to visualize near-wall and outer flow regions within the film. A novel camera system which translates in tandem with the moving bubble structure could be utilized. Temporal and unit-cell effects in slug flow BL evolution should be investigated; for example, development of free-stream velocity for fixed pipe locations. A BL growth model must be derived specifically for open-channel geometry and 3-dimensional effects require further research attention.
5. The novel slug-annular transitional framework posited here deserves subsequent devoted inquiry, both qualitative and quantitative. The dual-mechanism methodology can be investigated using high-resolution filmography focused on upstream pipe segments under operational conditions straddling the slug-annular boundary at a wide range of  $\mu_L$ -values. If deemed credible, clarification on  $\mu_L$ -range applicability is desirable and intensive mathematical derivation is needed to yield practical numerical models.

## Appendix A. Extracted data

Case	$\mu_L$ (mPas)	$Fr$	$\gamma$	D (mm)	$\lambda_{1D}^\circ$	$\lambda_{2D}^\circ$	$\lambda_N^\circ$	$\lambda_B^\circ$	$\lambda_T^\circ$	INT	BUB	TYPE
1.1	1.0	1.00	1.00	26	1.54	1.54	14.45	-	0.00	S	N	NC
1.2	5.5	1.00	1.00	26	2.06	2.21	19.64	-	0.00	S	N	NC
1.3	10.3	1.00	1.00	26	6.17	2.83	34.04	-	0.00	S	N	PC
1.4	15.4	1.00	1.00	26	6.68	3.50	36.81	-	0.00	S	N*	PC
1.5	20.3	1.00	1.00	26	6.53	3.34	33.62	-	0.00	S	N	PC
1.6	30.4	1.00	1.00	26	6.99	4.22	33.57	-	1.61	S	N	PC
2.1	1.0	1.50	-	26	2.57	1.44	28.38	-	-	S	N	-
2.2	5.5	1.50	-	26	3.96	2.31	22.57	-	-	S	N*	-
2.3	10.3	1.50	-	26	8.28	3.75	31.05	-	-	S	N*	-
2.4	15.4	1.50	-	26	6.02	3.44	29.67	-	-	S	N	-
2.5	20.3	1.50	-	26	8.79	4.68	35.17	-	-	S	N	-
2.6	30.4	1.50	-	26	10.33	5.60	36.50	-	-	S	N	-
3.1	1.0	2.00	-	26	4.06	1.59	34.91	-	0.00	T	N*	PC
3.2	5.5	2.00	-	26	6.27	2.88	24.99	-	0.00	T	N*	PC
3.3	10.3	2.00	-	26	5.91	2.88	24.94	-	3.35	S	N*	FC
3.4	15.4	2.00	-	26	10.69	5.91	40.26	-	0.00	S	N*	PC
3.5	20.3	2.00	-	26	9.56	6.53	32.85	-	0.00	S	N*	PC
3.6	30.4	2.00	-	26	14.70	9.77	39.95	-	2.69	S	N*	PC
4.1	1.0	3.00	-	26	2.67	1.29	34.04	-	0.00	W	Y	PC
4.2	5.5	3.00	-	26	9.61	7.71	37.94	-	0.00	W	Y	PC
4.3	10.3	3.00	-	26	9.82	5.55	44.58	-	0.00	W	Y	PC
4.4	15.4	3.00	-	26	14.14	11.05	41.03	-	0.00	S	Y	PC
4.5	20.3	3.00	-	26	12.24	7.30	41.70	-	0.00	S	Y	PC
4.6	30.4	3.00	-	26	16.14	14.09	42.21	-	0.00	S	Y	PC
5.1	1.0	4.00	-	26	7.10	2.42	36.50	-	0.00	W	Y	PC
5.2	5.5	4.00	-	26	7.76	7.51	41.34	-	5.95	W	Y	FC
5.3	10.3	4.00	-	26	7.46	8.33	35.84	-	3.49	W	Y	FC
5.4	15.4	4.00	-	26	11.36	7.10	42.52	-	3.41	W	Y	FC
5.5	20.3	4.00	-	26	16.71	6.38	57.02	-	4.58	W	Y	FC
5.6	30.4	4.00	-	26	19.85	11.72	46.63	-	2.64	S	Y	FC
A.1	37.7	1.92	3.25	20	13.69	9.41	40.61	1.17	2.61	S	N*	PC
A.2	37.7	3.23	0.78	20	20.50	13.41	52.46	7.88	6.44	S	Y	FC
B.1	352	1.81	3.00	20	17.33	14.58	43.66	10.80	10.86	S	Y	FC
B.2	352	2.94	0.59	20	22.01	17.61	50.38	9.51	11.03	S	Y	FC
C.1	352	0.68	0.50	20	11.91	-	43.85	-	11.79	S	Y	FC
$\Omega$ .1	510	0.57	1.00	50.8	10.33	-	45.68	-	4.68	S	Y	FC
$\Omega$ .2	680	0.57	1.00	50.8	13.10	-	46.04	-	7.59	S	Y	FC
$\Omega$ .3	960	0.57	1.00	50.8	14.76	-	47.50	-	8.31	S	Y	FC

Table A.6: All data extracted from N23 (i.j), S24 (m.k) and K20 ( $\Omega$ .q).  $\lambda^\circ$ -values in %.

**INT**: tortuosity of (lower) gas-liquid interface  
 S  $\rightarrow$  smooth  
 T  $\rightarrow$  transitional  
 W  $\rightarrow$  wavy  
**BUB**: presence-level of dispersed bubbles in film region  
 N  $\rightarrow$  none  
 N\*  $\rightarrow$  near-negligible  
 Y  $\rightarrow$  significant  
**TYPE**: type of bubble centring (see §2.1)  
 NC  $\rightarrow$  no-centring  
 PC  $\rightarrow$  partial-centring  
 FC  $\rightarrow$  full-centring

Figure A.25: Partial legend for table A.6.

## Appendix B. Additional centring plots

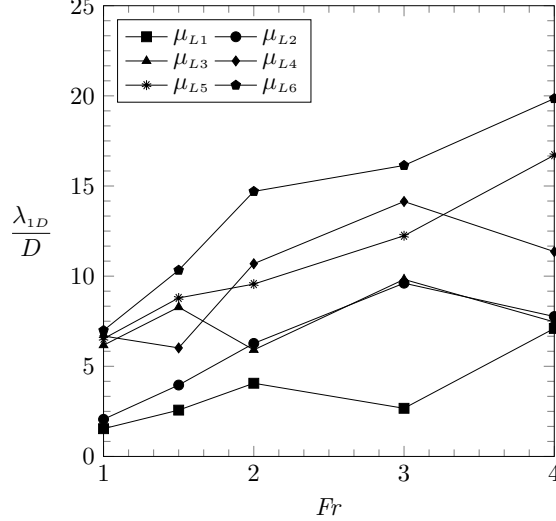


Figure B.26: Bubble centring data extracted from Naidek et al. (2023) (N23 dataset): Normalized  $\lambda_{1D}$  (%) as a function of  $Fr$  for fixed values of  $\mu_L$ .  $\mu_{L1} = 1\text{mPa s}$ ;  $\mu_{L2} = 5.5\text{mPa s}$ ;  $\mu_{L3} = 10.3\text{mPa s}$ ;  $\mu_{L4} = 15.4\text{mPa s}$ ;  $\mu_{L5} = 20.3\text{mPa s}$ ;  $\mu_{L6} = 30.4\text{mPa s}$ .

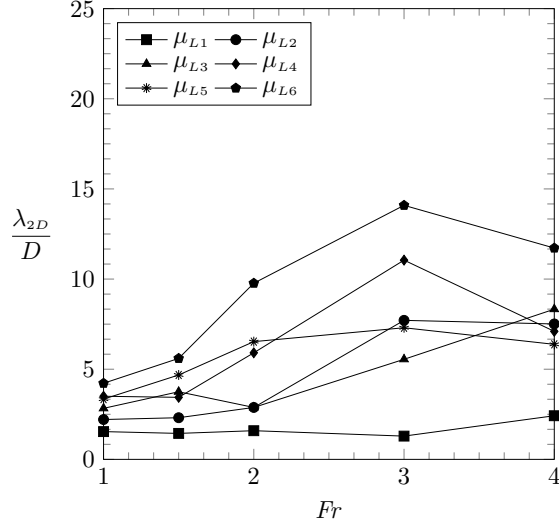


Figure B.27: Bubble centring data extracted from [Naidek et al. \(2023\)](#) (N23 dataset): Normalized  $\lambda_{2D}$  (%) as a function of  $Fr$  for fixed values of  $\mu_L$ .  $\mu_{L1} = 1\text{mPa s}$ ;  $\mu_{L2} = 5.5\text{mPa s}$ ;  $\mu_{L3} = 10.3\text{mPa s}$ ;  $\mu_{L4} = 15.4\text{mPa s}$ ;  $\mu_{L5} = 20.3\text{mPa s}$ ;  $\mu_{L6} = 30.4\text{mPa s}$ .

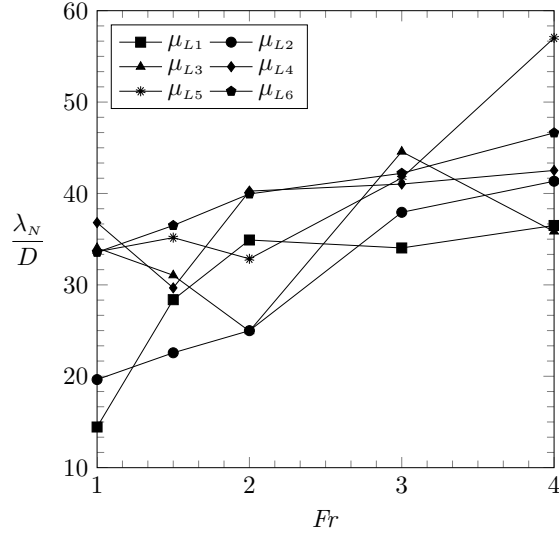


Figure B.28: Bubble centring data extracted from [Naidek et al. \(2023\)](#) (N23 dataset): Normalized  $\lambda_N$  (%) as a function of  $Fr$  for fixed values of  $\mu_L$ .  $\mu_{L1} = 1\text{mPa s}$ ;  $\mu_{L2} = 5.5\text{mPa s}$ ;  $\mu_{L3} = 10.3\text{mPa s}$ ;  $\mu_{L4} = 15.4\text{mPa s}$ ;  $\mu_{L5} = 20.3\text{mPa s}$ ;  $\mu_{L6} = 30.4\text{mPa s}$ .

## Appendix C. List of acronyms

- B87** Barnea (1987) mechanistic flow pattern transition model/study
- BL** Boundary layer
- G08** Gokcal et al. (2008) experimental HVL flow pattern study
- HVL** High-viscosity liquid  $\mu_L > 1\text{mPa}\cdot\text{s}$  ( $\mu_L \geq 5.5\text{mPa}\cdot\text{s}$  studied here)
- K20** Kim et al. (2020) HVL bubble centring dataset
- N23** Naidek et al. (2023) HVL bubble centring dataset
- PCV** Pipe control volume (from phasic inlet to outlet)
- PL20** Perkins and Li (2020) elongated bubble centring study/model
- S24** Shin et al. (2024) HVL bubble centring dataset
- SG00** Schlichting and Gersten (2000) textbook on boundary layer theory
- TB90** Taitel and Barnea (1990) mechanistic unit-cell slug model
- TD76** Taitel and Dukler (1976) mechanistic flow pattern transition model/study
- Z03** Zhang et al. (2003) mechanistic flow pattern transition model/study
- Z03M** Modified version of Z03 flow pattern transition model (from G08)

## Declaration of competing interests

There are no known conflicts of interest associated with this publication and no financial support that could have influenced its outcome.

## Acknowledgements

The author expresses gratitude for partial financial support, during the creation of this publication, stemming from a Discovery Grant from the Natural Sciences and Engineering Research Council of Canada (NSERC) (Grant No. NSERC RGPIN-2020-04571). I further thank my doctoral supervisor Huazhou Li for granting me support and full reign over my research endeavours, along with those who have never stopped believing in me.

## References

- Al-Safran, E.M., Al-Qenae, K., 2018. A study of flow-pattern transitions in high-viscosity oil-and-gas two-phase flow in horizontal pipes. *SPE Prod. Oper.* 33, 269–280.
- Al-Safran, E.M., Gokcal, B., Sarica, C., 2013. Investigation and prediction of high-viscosity liquid effect on two-phase slug length in horizontal pipelines. *SPE Prod. Oper.* 28, 296–305.
- Al-Safran, E.M., Kora, C., Sarica, C., 2015. Prediction of slug liquid holdup in high viscosity liquid and gas two-phase flow in horizontal pipes. *J. Pet. Sci. Eng.* 133, 566–575.
- Baker, O., 1954. Simultaneous flow of oil and gas. *Oil Gas J.* 53, 185–195.
- Barnea, D., 1986. Transition from annular flow and from dispersed bubble flow—unified models for the whole range of pipe inclinations. *Int. J. Multiphase Flow* 12, 733–744.
- Barnea, D., 1987. A unified model for predicting flow-pattern transitions for the whole range of pipe inclinations. *Int. J. Multiphase Flow* 13, 1–12.
- Barnea, D., Brauner, N., 1985. Holdup of the liquid slug in two phase intermittent flow. *Int. J. Multiphase Flow* 11, 43–49.
- Barnea, D., Shoham, O., Taitel, Y., 1982a. Flow pattern transition for downward inclined two phase flow: Horizontal to vertical. *Chem. Eng. Sci.* 37, 735–740.
- Barnea, D., Shoham, O., Taitel, Y., 1982b. Flow pattern transition for vertical downward two phase flow. *Chem. Eng. Sci.* 37, 741–744.
- Belt, R.J., Leinan, P.R., 2015. Measurement of mean velocity profiles in the slug and liquid film of gas-liquid slug flow, in: 17th International Conference on Multiphase Production Technology, BHR Group, Cannes, France. pp. 233–251.
- Bendiksen, K.H., 1984. An experimental investigation of the motion of long bubbles in inclined tubes. *Int. J. Multiphase Flow* 10, 467–483.

- Benjamin, T.B., 1968. Gravity currents and related phenomena. *J. Fluid Mech.* 31, 209–248.
- Blasius, H., 1908. Grenzschichten in flüssigkeiten mit kleiner reibung [The boundary layers in fluids with little friction]. *ZAMPDB* 56, 1–37.
- Chapra, S.C., 2012. *Applied Numerical Methods with MATLAB for Engineers and Scientists*. 3rd ed., McGraw-Hill, New York, USA.
- Diaz, M.J.C., 2016. Two-Phase Slug Flow Experiments with Viscous Liquids. PhD thesis. Norwegian University of Science and Technology. Trondheim, Norway. Available at <https://ntnuopen.ntnu.no/ntnu-xmlui/handle/11250/2390031>.
- Dong, X., Liu, H., Chen, Z., 2021. *Hybrid Enhanced Oil Recovery Processes for Heavy Oil Reservoirs*. 1st ed., Elsevier.
- Dukler, A.E., Hubbard, M.G., 1975. A model for gas-liquid flow in horizontal and near horizontal tubes. *Ind. Eng. Chem.* 14, 337–347.
- Gokcal, B., Al-Sarkhi, A.S., Sarica, C., 2009. Effects of high oil viscosity on drift velocity for horizontal and upward inclined pipes. *SPE Proj., Facil., Constr.* 4, 32–40.
- Gokcal, B., Wang, Q., Zhang, H.Q., Sarica, C., 2008. Effects of high oil viscosity on oil/gas flow behavior in horizontal pipes. *SPE Proj., Facil., Constr.* 3, 1–11.
- Islam, M.R., 2023. *Pipelines: Emerging Technologies and Design Criteria*. 1st ed., Gulf Professional Publishing, Cambridge, USA.
- Jamari, S., Hale, C.P., Hewitt, G.F., Richardson, S.M., 2008. Studies of the slug-annular regime transition in two-phase flow in horizontal pipes. *Multiphas. Sci. Tech.* 20, 1–24.
- Jeyachandra, B.C., Gokcal, B., Al-Sarkhi, A., Sarica, C., Sharma, A.K., 2012. Drift-velocity closure relationships for slug two-phase high-viscosity oil flow in pipes. *SPE J.* 17, 593–601.
- Kim, H.G., Kim, S.M., 2023. Slug flow characteristics of air-liquid two-phase flow in horizontal pipes over a wide range of liquid viscosities. *Int. J. Heat Mass Transf.* 208, 1–15.

- Kim, T.W., Al-Safran, E., Pereyra, E., Sarica, C., 2020. Experimental study using advanced diagnostics to investigate slug aeration and bubble behavior in high liquid viscosity horizontal slug flow. *J. Pet. Sci. Eng.* 191, 1–18.
- Kora, C., Sarica, C., Zhang, H.Q., Al-Sarkhi, A., Al-Safran, E., 2011. Effects of high oil viscosity on slug liquid holdup in horizontal pipes, in: *Canadian Unconventional Resources Conference, Society of Petroleum Engineers (SPE)*, Calgary, Canada. pp. 1–15.
- Lockhart, R.W., Martinelli, R.C., 1949. Proposed correlation data for isothermal two-phase, two-component flow in pipes. *Chem. Eng. Prog.* 45, 39–48.
- Mandhane, J.M., Gregory, G.A., Aziz, K., 1974. A flow pattern map for gas-liquid flow in horizontal pipes. *Int. J. Multiphase Flow* 1, 537–553.
- Matsubara, H., Naito, K., 2011. Effect of liquid viscosity on flow patterns of gas-liquid two-phase flow in a horizontal pipe. *Int. J. Multiphase Flow* 37, 1277–1281.
- McCain, W.D., 1990. *The Properties of Petroleum Fluids*. 2nd ed., PennWell Books, Tulsa, USA.
- Naidek, B.P., Conte, M.G., Cozin, C., dos Santos, E.N., Rodrigues, H.T., da Fonseca Jr., R., da Silva, M.J., Morales, R.E.M., 2023. Experimental study of influence of liquid viscosity in horizontal slug flow. *Exp. Therm. Fluid Sci.* 141, 1–11.
- Nicklin, D.J., Wilkes, J.O., Davidson, J.F., 1962. Two-phase flow in vertical tubes. *Trans. Instn. Chem. Engrs.* 40, 61–67.
- de Oliveira, W.R., de Paula, I.B., Martins, F.J.W.A., Farias, P.S.C., Azevedo, L.F.A., 2015. Bubble characterization in horizontal air-water intermittent flow. *Int. J. Multiphase Flow* 69, 18–30.
- Perkins, S.J., Li, H.A., 2020. Elongated bubble centring in horizontal gas-liquid slug flow. *Int. J. Multiphase Flow* 123, 1–20.
- Pope, S.B., 2000. *Turbulent Flows*. 1st ed., Cambridge University Press.
- Schlichting, H., Gersten, K., 2000. *Boundary-Layer Theory*. 8th ed., Springer, Berlin, Germany.

- Shin, H.C., Kim, S.H., Shah, Y., Kim, S.M., 2024. An experimental study on air-oil flow patterns in horizontal pipes using two synthetic oils. *Int. J. Heat Mass Transf.* 226, 1–19.
- Shippen, M., Bailey, W.J., 2012. Steady-state multiphase flow—past, present, and future, with a perspective on flow assurance. *Energy Fuels* 26, 4145–4157.
- Shoham, O., 2006. Mechanistic Modeling of Gas-Liquid Two-Phase Flow in Pipes. Society of Petroleum Engineers (SPE).
- Taitel, Y., Barnea, D., 1990. Two-phase slug flow. *Adv. Heat Transf.* 20, 83–132.
- Taitel, Y., Dukler, A., 1977. A model for slug frequency during gas-liquid flow in horizontal and near horizontal pipes. *Int. J. Multiphase Flow* 3, 585–596.
- Taitel, Y., Dukler, A.E., 1976. A model for predicting flow regime transitions in horizontal and near horizontal gas-liquid flow. *AIChE J.* 22, 47–55.
- Taitel, Y., Lee, N., Dukler, A.E., 1978. Transient gas-liquid flow in horizontal pipes: Modeling the flow pattern transitions. *AIChE J.* 24, 920–934.
- Tzotzi, C., Andritsos, N., 2013. Interfacial shear stress in wavy stratified gas-liquid flow in horizontal pipes. *Int. J. Multiphase Flow* 54, 43–54.
- Widyatama, A., Dinaryanto, O., Indarto, Deendarlianto, 2018. The development of image processing technique to study the interfacial behaviour of air-water slug two-phase flow in horizontal pipes. *Flow Meas. Instrum.* 59, 168–180.
- Zhang, H.Q., Sarica, C., Pereyra, E., 2012. Review of high-viscosity oil multiphase pipe flow. *Energy Fuels* 26, 3979–3985.
- Zhang, H.Q., Wang, Q., Sarica, C., Brill, J.P., 2003. Unified model for gas-liquid pipe flow via slug dynamics—part 1: Model development. *J. Energy Resour. Technol.* 125, 266–273.
- Zhao, Y., Lao, L., Yeung, H., 2015. Investigation and prediction of slug flow characteristics in highly viscous liquid and gas flows in horizontal pipes. *Chem. Eng. Sci.* 102, 124–137.

Zhao, Y., Yeung, H., Zorgani, E.E., Archibong, A.E., Lao, L., 2013. High viscosity effects on characteristics of oil and gas two-phase flow in horizontal pipes. *Chem. Eng. Sci.* 95, 343–352.

## Permissions

**Figure 4:** Reprinted from *Experimental Thermal and Fluid Science*, Vol. 141, Naidek, B. P., Conte, M. G., Cozin, C., dos Santos, E. N., Rodrigues, H. T., da Fonseca Jr., R., da Silva, M. J. and Morales, R. E. M., *Experimental study of influence of liquid viscosity in horizontal slug flow*, pp. 1-11, copyright 2023, with permission from Elsevier.

**Figure 5:** Reprinted from *International Journal of Heat and Mass Transfer*, Vol. 226, Shin, H.-C., Kim, S.-H., Shah, Y. and Kim, S.-M., *An experimental study on air-oil flow patterns in horizontal pipes using two synthetic oils*, pp. 1-19, copyright 2024, with permission from Elsevier.

**Figure 7:** Reprinted from *Journal of Petroleum Science and Engineering*, Vol. 191, Kim, T.-W., Al-Safran, E., Pereyra, E. and Sarica, C., *Experimental study using advanced diagnostics to investigate slug aeration and bubble behavior in high liquid viscosity horizontal slug flow*, pp. 1-18, copyright 2020, with permission from Elsevier.